CHALMERS
UNIVERSITY OF TECHNOLOGY

Fundamental Trade-Offs in Monostatic ISAC: A Holistic Investigation Toward 6G

Citation for the original published paper (version of record):
Keskin, M., Mojahedian, M., Lacruz, J. et al (2025). Fundamental Trade-Offs in Monostatic ISAC: A Holistic Investigation Toward 6G. IEEE Transactions on Wireless Communications, 24(9): 7856-7873. http://dx.doi.org/10.1109/TWC.2025.3563197

(article starts on next page)

Fundamental Trade-Offs in Monostatic ISAC: A Holistic Investigation Toward 6G

Musa Furkan Keskin, *Member, IEEE*, Mohammad Mahdi Mojahedian, *Member, IEEE*, Jesus O. Lacruz, Carina Marcus, Olof Eriksson, Andrea Giorgetti, *Senior Member, IEEE*, Joerg Widmer, *Fellow, IEEE*, and Henk Wymeersch, *Fellow, IEEE*

***Abstract*—This paper undertakes a holistic investigation of two fundamental trade-offs in monostatic OFDM integrated sensing and communication (ISAC) systems, namely, the time-frequency trade-off and the spatial trade-off, originating from the choice of modulation order for random data and the design of beamforming strategies, respectively. To counteract the elevated side-lobe levels induced by varying-amplitude data in high-order QAM signaling, we introduce a novel linear minimum mean-squared-error (LMMSE) estimator. We also provide a rigorous theoretical characterization of side-lobe levels achieved by the proposed LMMSE estimator and two benchmark schemes, proving its superiority for any modulation scheme and SNR level. Moreover, we explore spatial domain trade-offs through two ISAC transmission strategies: concurrent, employing joint beams, and time-sharing, using separate beams for sensing and communications not overlapping in time. Simulations demonstrate improved performance of the LMMSE estimator, especially in detecting weak targets in the presence of strong ones with high-order QAM, consistently yielding more favorable ISAC trade-offs than existing baselines under various modulation schemes, SNR conditions, RCS levels and transmission strategies. Additionally, we present experimental results to validate the effectiveness of the LMMSE estimator in reducing side-lobe levels, based on real-world measurements.**

***Index Terms*—OFDM, ISAC, monostatic sensing, LMMSE estimator, time-frequency trade-off, spatial trade-off, concurrent transmission, time-sharing transmission.**

I. Introduction

A. Background and Motivation

As RESEARCH and standardization efforts for 6G intensify, integrated sensing and communications (ISAC) stands out as a key enabler that can facilitate high-quality connectivity and endow networks with intrinsic sensing capability [1], [2], [3]. Such a convergence can revolutionize network functionalities that extend beyond traditional communication-only paradigms by making sensing a fundamentally built-in component rather than an add-on feature [4], [5]. In ISAC configurations, the monostatic approach is gaining momentum, especially given its ability to exploit the entire communication data for sensing purposes and its potential to mitigate the stringent synchronization challenges arising in bistatic and multistatic systems [6], [7], [8], [9]. Among various waveform candidates for ISAC implementation, the orthogonal frequency-division multiplexing (OFDM) waveform emerges as a natural choice owing to its widespread adoption across current wireless standards such as 5G, 5G-Advanced, WiFi/WLAN and DVB-T [10]. The inherent characteristics of OFDM, including its high spectral efficiency, immunity to multipath effects, high-accuracy and low-complexity radar operation and design flexibility, make it an ideal choice for ISAC applications [11], [12], [13], [14].

In the context of monostatic ISAC, OFDM radar sensing with 5G waveforms has recently received increasing attention [6], [15], [16], [17], [18], [19], [20]. Evaluations have been conducted on the sensing performance of a base station (BS) acting as a monostatic radar with downlink 5G new radio (NR) OFDM signals, focusing on the use of pilot/reference symbols alone [15], [18] as well as a combination of pilot/reference and data symbols [6], [16]. To achieve satisfactory target detection performance with sparse pilots, maintaining low side-lobe levels and eliminating ambiguities become critical in 5G/6G OFDM sensing [20]. In [15] and [17], various 5G signals and channels, including SSB, PRS, PDSCH and CSI-RS, have been investigated in terms of their delay-Doppler ambiguity function (AF) characteristics. Similarly, the study in [16] evaluates tracking performance using 5G NR signals within V2X networks, leading to guidelines on the design of 5G-Advanced and 6G frame structures [15], [16]. Overall, these studies highlight the significant potential of employing OFDM waveforms for sensing purposes, while also noting the challenges associated with target detection due to suboptimal side-lobe performance.

Another major challenge pertaining to side-lobe levels in monostatic OFDM sensing emerges from the use of random communication data [14], [21], [22]. This issue unveils a crucial inherent trade-off in monostatic OFDM ISAC systems, namely *the time-frequency trade-off*, falling under the umbrella of deterministic-random trade-offs [3], [23]. The time-frequency trade-off stems from the choice of modulation order for random data: higher-order QAM enhances

Received 25 July 2024; revised 8 January 2025; accepted 14 April 2025. Date of publication 29 April 2025; date of current version 15 September 2025. This work was supported in part by the Vinnova RADCOM2 Project under Grant 2021-02568, in part by the Smart Networks and Services (SNS) Joint Undertaking (JU) Project 6G-Distributed Intelligent Sensing and Communications (DISAC) under the EU's Horizon Europe Research and Innovation Program under Grant 101139130, in part by the Swedish Research Council (VR) through the Project 6G-PERCEF under Grant 2024-04390, and in part by European Union under Italian National Recovery and Resilience Plan (NRRP) of NextGenerationEU partnership on "Telecommunications of the Future" (Program RESTART) under Grant PE00000001. The associate editor coordinating the review of this article and approving it for publication was J. Wang. *(Corresponding author: Musa Furkan Keskin.)*

Musa Furkan Keskin, Mohammad Mahdi Mojahedian, and Henk Wymeersch are with the Department of Electrical Engineering, Chalmers University of Technology, SE 41296 Gothenburg, Sweden (e-mail: furkan@chalmers.se).

Carina Marcus and Olof Eriksson are with Magna Electronics Sweden AB, SE 44737 Vårgårda, Sweden.

Jesus O. Lacruz and Joerg Widmer are with IMDEA Networks, 28918 Madrid, Spain.

Andrea Giorgetti is with CNIT/WiLab and the Department of Electrical, Electronic, and Information Engineering "Guglielmo Marconi," University of Bologna, 40126 Bologna, Italy.

Digital Object Identifier 10.1109/TWC.2025.3563197

communication rates but compromises sensing performance, as the random, non-constant-modulus data leads to elevated side-lobe levels [14]. On the other hand, employing constant-modulus QPSK minimizes side-lobe levels, enhancing sensing performance but at the cost of lower communication rates. To explore and enhance the time-frequency trade-off, various transmit optimization schemes have been recently proposed, focusing on OFDM [14], [21], [24] as well as generic communication systems (along the lines of broader deterministic-random trade-offs) [23], [25], [26]. In [23], [24], and [26], multiple ISAC trade-off optimization problems have been formulated to optimize the input data distribution for improving the time-frequency trade-off. Considering MIMO-OFDM ISAC systems, [21] designs a symbol-level transmit precoder to minimize the range-Doppler integrated side-lobe level under multi-user communication quality-of-service (QoS) constraints. Similarly, the work in [14] proposes a probabilistic constellation shaping (PCS) approach to maximize the achievable rate under constraints on the variance of the radar AF with random OFDM data.

B. Research Gaps

Despite extensive research into sensing algorithms [6], [15], [16], [17], [18], [19] and trade-off analysis [14], [21], [23], [24], [25], [26] in OFDM ISAC systems, a number of crucial topics remain unexplored. First, previous studies on OFDM sensing have typically utilized QPSK signaling [6], [15], [17], [21], which compromises communication performance, or have implemented QAM data with reciprocal filtering (RF) [11], [16], [19], [27], which leads to elevated side-lobe levels at low SNRs due to enhanced noise power [21]. On the other hand, employing matched filtering (MF) [27] with QAM signaling as an alternative to RF results in increased side-lobe levels at high SNRs, caused by varying-amplitude data. Hence, no universally effective sensing algorithm exists that maintains robust performance across a wide range of SNR conditions, particularly when dealing with high-order modulations in monostatic OFDM ISAC systems. Moreover, prior works on time-frequency trade-off analysis focus exclusively on ISAC *transmit* signal optimization [14], [21], [23], [24], [25], [26] without tackling the problem of sensing *receiver* design. This leads to several drawbacks as optimizing transmitter design to tune ISAC trade-offs may hamper communication functionality and necessitate conveying additional control information to the communication receiver for symbol decoding, thereby increasing overhead. Conversely, the receiver design strategy adopted in this paper aligns with the *opportunistic sensing* paradigm [28], which does not interfere with the communication system. Finally, the *spatial trade-off*, resulting from the design of ISAC beamformers (e.g., [6], [29]), has been rarely studied alongside the time-frequency trade-off, which merits further investigation considering their complex interplay within various transmission schemes, such as *concurrent* and *time-sharing* [30].

In light of the existing literature on monostatic ISAC systems, several fundamental questions remain unanswered:

- How can robust sensing algorithms be designed for monostatic OFDM ISAC systems, accommodating known yet *varying-amplitude random data symbols* in the time-frequency domain generated by high-order modulation schemes? To what extent can we mitigate the *masking effect* in both single- and multi-target environments, resulting from increased side-lobe levels induced by non-constant-modulus data?
- What spatial domain trade-offs arise from the choice of ISAC transmit beamformers? How do different transmission strategies, namely, *concurrent and time-sharing transmission*, perform under various settings concerning the sensing algorithm, percentage of sensing-dedicated pilots and modulation order of random data?
- Given the inherent tension between sensing and communication (S&C) in time-frequency and spatial domains, how can communication data rates and accompanying ISAC trade-offs be realistically evaluated under different modulations and power allocations between S&C beams?

C. Contributions

With the aim of addressing the identified research gaps towards 6G, this study performs a comprehensive investigation of fundamental trade-offs in monostatic OFDM ISAC systems by introducing novel sensing algorithms, beamforming/transmission strategies and holistic performance evaluations using both simulated and experimental data. The main contributions can be summarized as follows:

- **Sensing with Varying-Amplitude Data in OFDM ISAC (Time-Frequency Trade-Offs):** We introduce a novel MIMO-OFDM radar sensing algorithm based on an LMMSE estimate of the time-frequency domain radar channel, specifically tailored for detection with varying-amplitude random communication data in monostatic ISAC systems. The proposed algorithm can effectively suppress high side-lobes induced by varying-amplitude data and significantly improve detection capability for weak targets, outperforming the conventional OFDM sensing algorithms (i.e., MF and RF [6], [11], [19], [27]).
- **Theoretical Characterization of Side-lobe Levels:** We provide a rigorous theoretical characterization of side-lobe levels obtained by the proposed LMMSE estimator as well as RF and MF benchmarks, valid for any modulation scheme and SNR level, yielding valuable insights into their sensing performance under different SNR regimes and modulation orders.
- **ISAC Transmission Strategies (Spatial Trade-Offs):** To analyze the spatial domain trade-offs, we investigate two ISAC transmission strategies: concurrent transmission, where the same beam is used for S&C, and time-sharing transmission, which uses dedicated beams for S&C non-overlapping in time. We also introduce a mutual information (MI) approximation method that leverages Monte Carlo sampling techniques to evaluate data rates (with imperfect knowledge of channel) and the resulting ISAC trade-offs under various modulation schemes.
- **Holistic Performance Investigation via Simulations and Experiments:** To offer comprehensive guidelines for

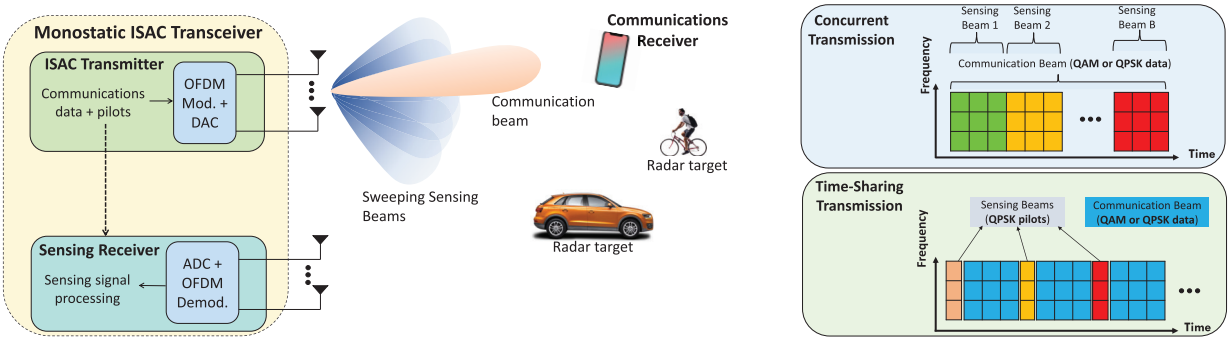

Fig. 1. Monostatic ISAC system featuring a monostatic ISAC transceiver, which integrates an ISAC transmitter and a sensing receiver on the same hardware platform, and a communications receiver on a separate device. In concurrent transmission, sensing receiver utilizes all communication data, with transmit power distributed between sensing and communication beams. In time-sharing transmission, dedicated sensing and communications beams are transmitted in a time-multiplexed fashion.

the design of 6G systems, we carry out extensive simulations to investigate fundamental ISAC trade-offs within the time-frequency and spatial domains under a wide array of transmission settings and channel conditions, including modulation order, SNR and power/time allocation between S&C. The proposed LMMSE estimator demonstrates substantial improvements in the trade-offs between probability of detection and achievable rate compared to existing baselines. We also provide experimental results to verify the effectiveness of the LMMSE estimator on real measurements.

II. System Model and Problem Description

Consider a monostatic OFDM ISAC system consisting of two entities, as shown in Fig. 1: a multiple-antenna dual-functional ISAC transceiver and a single-antenna communications receiver (RX). The ISAC transceiver contains *(i)* an ISAC transmitter (TX) with an N_{T}-element uniform linear array (ULA) that sends data/pilot symbols to the communications RX and *(ii)* a sensing RX with an N_{R}-element ULA that performs radar sensing by processing the backscattered signals for target detection, estimation and tracking [2], [4], [11]. In the monostatic configuration under consideration, the sensing RX is co-located on the same device as the ISAC TX, thereby sharing the same oscillator and having access to the entire OFDM transmit signal [6], [8], [31]. To ensure that the sensing RX experiences no self-interference during full-duplex operation, we assume that the TX/RX antennas at the ISAC transceiver are sufficiently isolated [4], [7], [11], [32], [33], [34], [35]. In this section, we introduce the OFDM transmit signal model, different ISAC transmission/beamforming strategies and provide received signal models at both the sensing and communication RXs. Additionally, we formulate the problems of interest tackled throughout the paper.

A. Transmit Signal Model

We consider an OFDM frame with N subcarriers and M symbols. The complex baseband transmit signal for the m^{th} symbol can be expressed as [6] and [11]

$$s_m(t) = \frac{1}{\sqrt{N}} \sum_{n=0}^{N-1} x_{n,m}\, e^{j2\pi n \Delta f t} g\left(\frac{t - mT_{\mathrm{sym}}}{T_{\mathrm{sym}}}\right), \quad (1)$$

where $x_{n,m}$ is the data/pilot on the n^{th} subcarrier and the m^{th} symbol, $\Delta f = 1/T$ is the subcarrier spacing with T representing the elementary symbol duration, $T_{\mathrm{sym}} = T + T_{\mathrm{cp}}$ is the total symbol duration including the cyclic prefix (CP) T_{cp}, and $g(t)$ is a rectangular pulse that takes the value 1 for $t \in [0, 1]$ and 0 otherwise. Employing single-stream beamforming [6], [34], [36], the passband transmit signal over the TX array for the entire OFDM frame is given by

$$\Re\left\{\sum_{m=0}^{M-1} \mathbf{f}_m s_m(t) e^{j2\pi f_c t}\right\}, \quad (2)$$

where $\mathbf{f}_m \in \mathbb{C}^{N_{\mathrm{T}} \times 1}$ is the TX beamforming (BF) vector applied for the m^{th} symbol and f_c is the carrier frequency. Denoting by P_{T} the transmit power, we set $\|\mathbf{f}_m\|^2 = P_{\mathrm{T}}\, \forall m$ and $\mathbb{E}\{|x_{n,m}|^2\} = 1$.

B. ISAC Transmission Strategies

We investigate two ISAC transmission strategies concerning the choice of $x_{n,m}$ and $\mathbf{f}_m$ in (2).

1) Concurrent Transmission: In the concurrent transmission, a common beam is utilized simultaneously for S&C. Inspired by [29, Thm. 2], we use the multibeam approach in which the TX BF vector employed at the m^{th} symbol is given by [6] and [37]

$$\mathbf{f}_m = \sqrt{\rho}\, \mathbf{f}_{m,\mathrm{s}} + \sqrt{1-\rho}\, \mathbf{f}_{m,\mathrm{c}}, \quad (3)$$

where $\mathbf{f}_{m,\mathrm{s}} \in \mathbb{C}^{N_{\mathrm{T}} \times 1}$ and $\mathbf{f}_{m,\mathrm{c}} \in \mathbb{C}^{N_{\mathrm{T}} \times 1}$ represent, respectively, the sensing and communication BF vectors, and $0 \leq \rho \leq 1$ denotes the ISAC weight that controls the trade-off between S&C. In this strategy, all $x_{n,m}$'s are assumed to be data symbols[1] intended for the communications RX, while the sensing RX exploits the entire frame for radar sensing. It has been proven in [29, Thm. 2] that the optimal ISAC beamformer that maximizes SNR at a given sensing location while satisfying a communication SINR constraint in a single user scenario lies in the subspace of sensing and

[1]For ease of exposition and analysis, the communication channel is assumed to be estimated a-priori, eliminating the need for pilot symbols. While the proposed framework can theoretically be extended to account for the impact of communication pilots on ISAC performance trade-offs, exploring this aspect is beyond the scope of the current study and is reserved for future research.

communication channels, which strongly motivates the use of the structure in (3) (i.e., a weighted combination of sensing and communication beamformers).

2) Time-Sharing Transmission: In the time-sharing transmission, dedicated beams for sensing and communications are used in non-overlapping time slots [30]. Thus, at each OFDM symbol, the ISAC TX transmits either a sensing beam or a communication beam. More formally,

$$\mathbf{f}_m = \begin{cases} \mathbf{f}_{m,\mathrm{s}}, & m \in \mathcal{S} \\ \mathbf{f}_{m,\mathrm{c}}, & m \in \mathcal{C} \end{cases}, \; x_{n,m} = \begin{cases} \text{pilot}, & m \in \mathcal{S} \\ \text{data}, & m \in \mathcal{C}, \end{cases} \tag{4}$$

where $\mathcal{S} \cup \mathcal{C} = \{0, \ldots, M-1\}$ and $\mathcal{S} \cap \mathcal{C} = \emptyset$. In (4), 'pilot' refers to dedicated *sensing pilots with unit amplitude* [38], whereas 'data' could be either unit-amplitude (e.g., QPSK) or varying-amplitude (e.g., QAM). The sensing RX utilizes only the pilots for sensing, while the communications rate might be compromised due to the replacement of a portion of data by pilots. The time-sharing ratio $|\mathcal{S}|/M$ allows tuning the trade-off between S&C.

C. Sensing Signal Model

Given (1) and (2), the backscattered signal at the sensing RX array over subcarrier n and symbol m after the CP removal and FFT operations can be written as [39]

$$\mathbf{y}_{n,m} = \mathbf{H}_{n,m}\mathbf{f}_m x_{n,m} + \mathbf{n}_{n,m} \in \mathbb{C}^{N_\mathrm{R}\times 1}, \tag{5}$$

where $\mathbf{H}_{n,m} \in \mathbb{C}^{N_\mathrm{R}\times N_\mathrm{T}}$ denotes the channel matrix at the n^{th} subcarrier and the m^{th} symbol, and $\mathbf{n}_{n,m} \in \mathbb{C}^{N_\mathrm{R}\times 1}$ is the additive white Gaussian noise (AWGN) component with $\mathbf{n}_{n,m} \sim \mathcal{CN}(\mathbf{0}, \sigma^2\mathbf{I})$ and $\sigma^2 = N_0 N \Delta f$, with N_0 representing the noise power spectral density (PSD). Considering the presence of K point targets in the environment, the sensing channel can be expressed as

$$\mathbf{H}_{n,m} = \sum_{k=0}^{K-1} \alpha_k e^{-j2\pi n \Delta f \tau_k} e^{j2\pi m T_{\mathrm{sym}} \nu_k} \mathbf{a}_\mathrm{R}(\theta_k)\mathbf{a}_\mathrm{T}^T(\theta_k), \tag{6}$$

where α_k, τ_k, ν_k and θ_k denote, respectively, the complex channel gain (including the effects of path attenuation and radar cross section (RCS)), round-trip delay, Doppler shift and angle-of-arrival (AOA)/angle-of-departure (AOD) of the k^{th} target. Here, $\tau_k = 2d_k/c$ and $\nu_k = 2v_k/\lambda$, with c, $\lambda = c/f_c$, d_k and v_k denoting the speed of propagation, the wavelength, the range and velocity of the k^{th} target, respectively. In addition, the channel gain is given by the radar range equation $|\alpha_k|^2 = \sigma_{\mathrm{rcs},k}\lambda^2/[(4\pi)^3 d_k^4]$ [40, Eq. (2.8)], where $\sigma_{\mathrm{rcs},k}$ denotes the RCS of the k^{th} target. Moreover, the ULA steering vectors are defined as

$$\mathbf{a}_\mathrm{T}(\theta) = \left[1 \; e^{j\frac{2\pi}{\lambda}d\sin(\theta)} \; \ldots \; e^{j\frac{2\pi}{\lambda}d(N_\mathrm{T}-1)\sin(\theta)}\right]^T, \tag{7}$$

$$\mathbf{a}_\mathrm{R}(\theta) = \left[1 \; e^{j\frac{2\pi}{\lambda}d\sin(\theta)} \; \ldots \; e^{j\frac{2\pi}{\lambda}d(N_\mathrm{R}-1)\sin(\theta)}\right]^T, \tag{8}$$

where $d = \lambda/2$ denotes the antenna element spacing.

D. Communications Signal Model

The signal received at the communications RX over subcarrier n and symbol m is given by

$$y_{n,m}^{\mathrm{com}} = (\mathbf{h}_{n,m}^{\mathrm{com}})^T \mathbf{f}_m x_{n,m} + z_{n,m} \in \mathbb{C}, \tag{9}$$

where $\mathbf{h}_{n,m}^{\mathrm{com}} \in \mathbb{C}^{N_\mathrm{T}\times 1}$ is the communication channel over subcarrier n and symbol m. In addition, $z_{n,m}$ is AWGN with $z_{n,m} \sim \mathcal{CN}(0, \sigma_\mathrm{c}^2)$. Assuming $\widetilde{K}$ paths between the ISAC TX and the communications RX, $\mathbf{h}_{n,m}^{\mathrm{com}}$ can be modeled as

$$\mathbf{h}_{n,m}^{\mathrm{com}} = \sum_{k=0}^{\widetilde{K}-1} \widetilde{\alpha}_k e^{-j2\pi n \Delta f \widetilde{\tau}_k} e^{j2\pi m T_{\mathrm{sym}} \widetilde{\nu}_k} \mathbf{a}_\mathrm{T}(\widetilde{\theta}_k), \tag{10}$$

where $\widetilde{\alpha}_k$, $\widetilde{\tau}_k$, $\widetilde{\nu}_k$ and $\widetilde{\theta}_k$ denote, respectively, the complex channel gain, delay, Doppler shift and AOD of the k^{th} path. Here, $k = 0$ represents the line-of-sight (LOS) path. Accordingly, the channel gains are given by $|\widetilde{\alpha}_0|^2 = \lambda^2/(4\pi\widetilde{d}_0)^2$ and $|\widetilde{\alpha}_k|^2 = \widetilde{\sigma}_{\mathrm{rcs},k}\lambda^2/[(4\pi)^3 \widetilde{d}_{k,1}^2 \widetilde{d}_{k,2}^2]$ for $k > 0$ [41, Eq. (45)], where $\widetilde{\sigma}_{\mathrm{rcs},k}$ denotes the RCS of the scatterer associated with the k^{th} path, $\widetilde{d}_{k,1}$ and $\widetilde{d}_{k,2}$ are the distances between TX-scatterer and scatterer-RX.

E. Beamformers for Sensing and Communications

To search for potential targets in the environment, the TX sensing beam $\mathbf{f}_{m,\mathrm{s}}$ in (3) and (4) sweeps an angular range $[-\theta_{\max}, \theta_{\max}]$. We assume the use of B different sensing beams over M symbols. Let $\mathcal{M}_b$ denote the set of indices of symbols for which the b^{th} beam is employed, i.e., $\mathcal{M}_1 = \{1, \ldots, M/B\}, \ldots, \mathcal{M}_B = \{M - M/B + 1, \ldots, M\}$. Hence, the sensing beams are given by $\mathbf{f}_{m,\mathrm{s}} = \sqrt{P_\mathrm{T}/N_\mathrm{T}}\mathbf{a}_\mathrm{T}^*(\theta_b)$ for $m \in \mathcal{M}_b$, where $\theta_b = -\theta_{\max} + 2(b-1)/(B-1)\theta_{\max}$.

For communications, we assume a LOS beam tracking scenario [42] where the TX communication beam $\mathbf{f}_{m,\mathrm{c}}$ in (3) and (4) is aligned with $\widetilde{\theta}_0$ and stays constant during the entire frame, i.e., $\mathbf{f}_{m,\mathrm{c}} = \sqrt{P_\mathrm{T}/N_\mathrm{T}}\mathbf{a}_\mathrm{T}^*(\widetilde{\theta}_0)\,\forall m$.

F. Impact of Non-Constant-Modulus Data on Sensing

To demonstrate the impact of different modulation orders on sensing performance, we provide an illustrative example of range profiles in Fig. 2, obtained with QPSK and 1024−QAM modulations. The range profiles are generated by applying reciprocal filtering and 2-D FFT based standard OFDM radar processing (e.g., [6], [11], [27], [33]). From the figure, it is evident that while high-order modulations provide high data rates, they also tend to result in elevated side-lobe levels, which significantly impairs the detection of weak targets. This example sheds light on one of the fundamental trade-offs in ISAC systems, namely the time-frequency trade-off, from the perspective of detection.

G. Problem Description

Given the OFDM frame $\mathbf{X} \in \mathbb{C}^{N\times M}$ with $[\mathbf{X}]_{n,m} = x_{n,m}$ consisting of random data (and, potentially, pilot symbols), the ISAC TX beamformers $\{\mathbf{f}_m\}_{m=0}^{M-1}$, and the sensing and communications models in (5) and (9), the problems of interest in this work are: *(i)* to develop a radar sensing algorithm

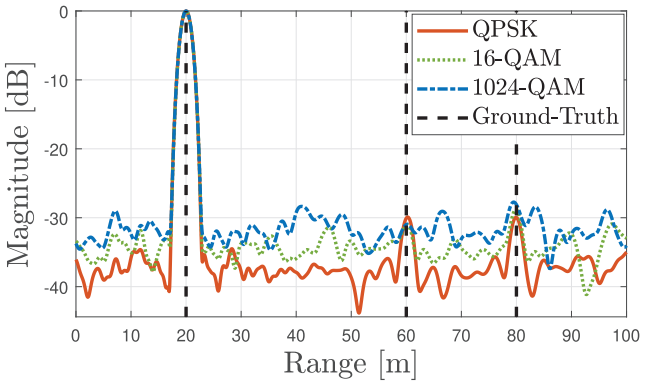

Fig. 2. Range profiles obtained via conventional OFDM radar processing based on reciprocal filtering (i.e., element-wise division of transmit symbols) and 2-D FFT [6], [11], [27], [33] with QPSK, 16−QAM and 1024−QAM modulations. The parameters employed are $B = 100\,\text{MHz}$, $M = 140$, with additional details as specified in Table II. The scenario involves three targets, each moving at $10\,\text{m/s}$, with RCSs of $(0, -10, -5)\,\text{dBsm}$ and located at ranges of $(20, 60, 80)\,\text{m}$ and angles of $(10°, 5°, 15°)$. It is observed that the use of communication data symbols from high-order modulations increases side-lobe levels, thereby masking the presence of weaker targets.

to detect the presence of multiple targets and estimate their delay-Doppler-angle parameters from 3-D tensor observations $\{\mathbf{y}_{n,m}\}$ in (5) over N_R receive antennas, N subcarriers and M symbols, *(ii)* to evaluate the data rate for the signal model in (9) across diverse modulation orders (e.g., QAM, QPSK), and *(iii)* to investigate ISAC trade-offs for different configurations of $\mathbf{X}$ and different choices of $\mathbf{f}_m$ (determined by the ISAC weight in (3), the data/pilot ratio in (4) and the modulation order in both strategies). We begin by tackling the first problem in Sec. III. The method to approximate the communication MI for data rate evaluation will be introduced in Sec. IV. Finally, we present simulation and experimental results to explore sensing and ISAC trade-off performances in Sec. V.

III. Radar Sensing Algorithm

In this section, we introduce a novel sensing algorithm for multiple target detection and accompanying parameter estimation using the observation in (5), that can account for arbitrary $\mathbf{X}$ and TX beam sweeping.

A. Beam-Specific Channel Estimation

Target detection from the observation (5) via *coherent* processing in the spatial-frequency-time domains involves a computationally demanding 3-D search over the delay-Doppler-angle tuples of potential targets [43], [44]. Furthermore, the beam sweeping procedure used for sensing, as discussed in Sec. II-E, results in varying gains for targets across different beams. This is because the overall gain of the k^th target in (6) is represented by $\alpha_k \mathbf{a}_\text{T}^T(\theta_k)\mathbf{f}_m$, which varies over symbols m when $\mathbf{f}_m$ changes [6].

Given these two challenges in detection/estimation from (5), we propose to formulate the problem of sensing as a series of *beam-specific channel estimation* problems where for each beam the time-frequency domain radar channel is estimated per RX element by treating it as an *unstructured channel* rather than a delay-Doppler parameterized one as in (6), followed by *noncoherent* integration [43], [44] of the resulting delay-Doppler images over the RX array. More formally, for the b^th beam, the sensing observations in (5) at the i^th RX element can be expressed using (6) as

$$\mathbf{Y}_{i,b} = \mathbf{H}_{i,b} \odot \mathbf{X}_b + \mathbf{N}_{i,b} \in \mathbb{C}^{N \times M_b}\,, \tag{11}$$

where $\odot$ denotes the Hadamard (element-wise) product,

$$\mathbf{H}_{i,b} \triangleq \sum_{k=0}^{K-1} \alpha_{b,k} \mathbf{b}(\tau_k)\mathbf{c}_b^H(\nu_k)[\mathbf{a}_\text{R}(\theta_k)]_i \in \mathbb{C}^{N \times M_b} \tag{12}$$

represents the time-frequency radar channel at the i^th RX element for the b^th beam, $\mathbf{X}_b = [\mathbf{X}]_{:,\mathcal{M}_b} \in \mathbb{C}^{N \times M_b}$ is the transmit symbols for the b^th beam, $\text{vec}\,(\mathbf{N}_{i,b}) \sim \mathcal{CN}(\mathbf{0}, \sigma^2\mathbf{I})$ and $M_b = |\mathcal{M}_b|$. In (12), $\alpha_{b,k} = \alpha_k \mathbf{a}_\text{T}^T(\theta_k)\widetilde{\mathbf{f}}_b$ denotes the overall gain of the k^th target for the b^th beam,

$$\mathbf{b}(\tau) \triangleq \left[1 \;\; e^{-j2\pi\Delta f \tau} \;\; \ldots \;\; e^{-j2\pi(N-1)\Delta f \tau}\right]^T\,, \tag{13}$$

$$\mathbf{c}(\nu) \triangleq \left[1 \;\; e^{-j2\pi T_\text{sym} \nu} \;\; \ldots \;\; e^{-j2\pi(M-1)T_\text{sym}\nu}\right]^T\,, \tag{14}$$

represent the frequency-domain and temporal (slow-time) steering vectors, respectively, and $\mathbf{c}_b(\nu) = [\mathbf{c}(\nu)]_{\mathcal{M}_b}$. Moreover, $\widetilde{\mathbf{f}}_b \in \mathbb{C}^{N_\text{T} \times 1}$ represents the b^th beam, i.e., $[\mathbf{F}]_{:,\mathcal{M}_b} = [\widetilde{\mathbf{f}}_b \ldots \widetilde{\mathbf{f}}_b] \in \mathbb{C}^{N_\text{T} \times M_b}$, with $\mathbf{F} \triangleq [\mathbf{f}_1 \ldots \mathbf{f}_m] \in \mathbb{C}^{N_\text{T} \times M}$ denoting the entire TX beamforming matrix.

We revisit the two commonly employed methods to estimate $\mathbf{H}_{i,b}$ from $\mathbf{Y}_{i,b}$ in (11) and present the proposed method.

1) Reciprocal Filtering (RF): The reciprocal filtering (RF) performs channel estimation by element-wise division of received symbols by transmit symbols [6], [11], [15], [27], [33]

$$\widehat{\mathbf{H}}_{i,b} = \mathbf{Y}_{i,b} \oslash \mathbf{X}_b\,, \tag{15}$$

where $\oslash$ denotes element-wise division. The RF estimator in (15) can be derived as a result of the least-squares (LS) solution in (11) and thus corresponds to the *zero-forcing* [45].

2) Matched Filtering (MF): The matched filtering (MF) approach aims to maximize the SNR at the output of the filter and applies conjugate multiplication of received symbols by transmit symbols[2] [27], [47]

$$\widehat{\mathbf{H}}_{i,b} = \mathbf{Y}_{i,b} \odot \mathbf{X}_b^*\,. \tag{16}$$

3) Proposed LMMSE Estimator: We propose to employ an LMMSE estimator to estimate $\mathbf{H}_{i,b}$ in (11) by treating it as a random unknown parameter as opposed to deterministic modeling in RF and MF strategies. To this end, let us assume that the vectorized version of the channel in (12), given by

$$\mathbf{h}_{i,b} \triangleq \text{vec}\,(\mathbf{H}_{i,b}) = \sum_{k=0}^{K-1} \alpha_{b,k}\mathbf{c}_b^*(\nu_k) \otimes \mathbf{b}(\tau_k)[\mathbf{a}_\text{R}(\theta_k)]_i\,, \tag{17}$$

has the following first and second moments:

$$\overline{\mathbf{h}}_{i,b} \triangleq \mathbb{E}\{\mathbf{h}_{i,b}\},\;\; \mathbf{C}_{i,b} \triangleq \mathbb{E}\{(\mathbf{h}_{i,b} - \overline{\mathbf{h}}_{i,b})(\mathbf{h}_{i,b} - \overline{\mathbf{h}}_{i,b})^H\}\,. \tag{18}$$

[2]The counterpart of the MF estimator in communications is represented by the *maximum ratio combining (MRC)* scheme [46, Eq. (2.35)], which performs equalization using channel coefficients to estimate data symbols while (16) removes the impact of data symbols to estimate the channel.

Based on (17), the vectorized observations in (11) can be written as

$$\mathbf{y}_{i,b} = \mathbf{D}_{i,b}\mathbf{h}_{i,b} + \mathbf{n}_{i,b}\,, \tag{19}$$

where $\mathbf{y}_{i,b} \triangleq \mathrm{vec}\,(\mathbf{Y}_{i,b})$, $\mathbf{D}_{i,b} \triangleq \mathrm{diag}\,(\mathrm{vec}\,(\mathbf{X}_b))$ and $\mathbf{n}_{i,b} \triangleq \mathrm{vec}\,(\mathbf{N}_{i,b})$. Given the statistics in (18), the LMMSE estimate of the radar channel $\mathbf{h}_{i,b}$ in (19) is given by [48, p. 389]

$$\begin{aligned}\widehat{\mathbf{h}}_{i,b} = \mathbf{C}_{i,b}\mathbf{D}_{i,b}^H(\mathbf{D}_{i,b}\mathbf{C}_{i,b}\mathbf{D}_{i,b}^H + \sigma^2\mathbf{I})^{-1} \\ \times\,(\mathbf{y}_{i,b} - \mathbf{D}_{i,b}\overline{\mathbf{h}}_{i,b}) + \overline{\mathbf{h}}_{i,b}\,.\end{aligned} \tag{20}$$

The following lemma helps simplification of (20).

Lemma 1 (OFDM Radar Channel Statistics): Suppose that the target parameters in the radar sensing channel (17) are distributed independently as $\alpha_{b,k} \sim \mathcal{CN}(0, \sigma^2_{\alpha_{b,k}})$, $\tau_k \sim \mathcal{U}[0, 1/\Delta f]$, $\nu_k \sim \mathcal{U}[0, 1/(f_c T_{\mathrm{sym}})]$, $\theta_k \sim \mathcal{U}[-\pi/2, \pi/2]$ *(i.e., delays, Dopplers and angles are drawn uniformly from their respective unambiguous detection intervals). In addition, different targets are assumed to have independent distributions*[3]*.Then, the statistics of* $\mathbf{h}_{i,b}$ *in (18) are given by* $\overline{\mathbf{h}}_{i,b} = \mathbf{0}$ *and* $\mathbf{C}_{i,b} = \sigma^2_{\alpha_b}\mathbf{I}$*, where* $\sigma^2_{\alpha_b} \triangleq \sum_{k=0}^{K-1} \sigma^2_{\alpha_{b,k}}$.

Proof: Please see Appendix A. ■

Based on Lemma 1, (20) becomes

$$\widehat{\mathbf{h}}_{i,b} = \sigma^2_{\alpha_b}\mathbf{D}_{i,b}^H(\sigma^2_{\alpha_b}\mathbf{D}_{i,b}\mathbf{D}_{i,b}^H + \sigma^2\mathbf{I})^{-1}\mathbf{y}_{i,b}\,. \tag{21}$$

Folding (21) back into matrix and plugging the definition of $\mathbf{D}_{i,b}$, the LMMSE channel estimate is given by[4]

$$\widehat{\mathbf{H}}_{i,b} = \frac{\mathbf{Y}_{i,b} \odot \mathbf{X}_b^*}{|\mathbf{X}_b|^2 + \mathrm{SNR}_b^{-1}}\,, \tag{22}$$

where $\mathrm{SNR}_b \triangleq \sigma^2_{\alpha_b}/\sigma^2$, and the $|\cdot|^2$ operation is performed element-wise.[5]

4) Interpretation of LMMSE Estimator: A comparative analysis of (22) with (15) and (16) yields the following insights:

- *At high SNRs*, i.e., as $\mathrm{SNR}_b \to \infty$, we have $\widehat{\mathbf{H}}_{i,b} \approx \mathbf{Y}_{i,b} \oslash \mathbf{X}_b$. Thus, the LMMSE estimator converges to the RF estimator in (15).
- *At low SNRs*, i.e., as $\mathrm{SNR}_b \to 0$, we obtain $\widehat{\mathbf{H}}_{i,b} \approx \mathbf{Y}_{i,b} \odot \mathbf{X}_b^*$. This suggests that the LMMSE estimator converges to the MF estimator in (16).

Hence, the LMMSE estimator represents a generalization of the RF and MF receivers to the entire SNR range. When using unit-amplitude modulations, where $|\mathbf{X}_b|$ is an all-ones matrix, all estimators become equivalent, regardless of the SNR level[6].

5) Theoretical Characterization of Side-Lobe Levels of Different Estimators: To quantify the side-lobe behavior of the RF, MF and LMMSE estimators across various SNR regimes and modulation orders, we provide several theoretical results regarding the peak-to-sidelobe level ratio (PSLR) achieved by these estimators. Here, the PSLR is defined as [52]

$$\mathrm{PSLR} = \frac{\mathbb{E}\{|\chi(\tau_0, \nu_0)|^2\}}{\mathbb{E}\{|\chi(\tau, \nu)|^2\}}\,,\ (\tau, \nu) \in \mathcal{R}\,, \tag{23}$$

where $\chi(\tau, \nu)$ is the delay-Doppler response corresponding to a certain OFDM radar receiver (e.g., RF, MF, LMMSE), (τ_0, ν_0) represents the delay-Doppler of the target of interest, and $\mathcal{R} = \{(\tau, \nu) \mid |\tau - \tau_0| \gg \Delta\tau, |\nu - \nu_0| \gg \Delta\nu\}$ denotes the asymptotic side-lobe region containing delay-Doppler cells located sufficiently far from the main-lobe at (τ_0, ν_0), with $\Delta\tau$ and $\Delta\nu$ denoting the resolution in delay and Doppler, respectively. The following results provide rigorous theoretical characterizations of side-lobe levels, applicable to any modulation and SNR level (dropping b for simplicity), as well as comparative analyses of the different estimators.

Proposition 1: The PSLR in (23) achieved by the different estimators under consideration is given by

$$\mathrm{PSLR}^{\mathrm{RF}} = 1 + NM\left(\mathbb{E}\left\{\frac{1}{|x|^2}\right\}\mathrm{SNR}^{-1}\right)^{-1}, \tag{24}$$

$$\mathrm{PSLR}^{\mathrm{MF}} = 1 + NM\left(\mathbb{E}\{|x|^4\} - 1 + \mathrm{SNR}^{-1}\right)^{-1}, \tag{25}$$

$$\mathrm{PSLR}^{\mathrm{LMMSE}} = 1 + NM\left(\left(\mathbb{E}\left\{\frac{|x|^2}{|x|^2 + \mathrm{SNR}^{-1}}\right\}\right)^{-1} - 1\right)^{-1} \tag{26}$$

where x represents the transmit symbol modeled as a complex random variable from a given discrete constellation with unit average power, i.e., $\mathbb{E}\{|x|^2\} = 1$.

Proof: Please see Appendix B. ■

Proposition 2: $\mathrm{PSLR}^{\mathrm{LMMSE}} \geq \mathrm{PSLR}^{\mathrm{RF}}$ *always holds.*

Proof: Please see Appendix C. ■

Proposition 3: $\mathrm{PSLR}^{\mathrm{LMMSE}} \geq \mathrm{PSLR}^{\mathrm{MF}}$ *always holds.*

Proof: Please see Appendix D. ■

Corollary 1: The PSLR of LMMSE converges to that of MF and RF at low and high SNRs, respectively, i.e.,

$$\lim_{\mathrm{SNR}\to 0} \mathrm{PSLR}^{\mathrm{LMMSE}} = \mathrm{PSLR}^{\mathrm{MF}}\,, \tag{27}$$

$$\lim_{\mathrm{SNR}\to \infty} \mathrm{PSLR}^{\mathrm{LMMSE}} = \mathrm{PSLR}^{\mathrm{RF}}\,. \tag{28}$$

Proof: The proof follows via first-order Taylor expansions. ■

[3]In each OFDM frame, we sample a realization from these distributions, which we assume to stay constant during the frame. We note that the resulting LMMSE channel estimate derived in (22) is valid for any arbitrary (non-Gaussian) distribution of $\alpha_{b,k}$ with zero mean and a variance of $\sigma^2_{\alpha_{b,k}}$. The zero-mean assumption generally holds since the phase induced by two-way propagation and target scattering is uniformly distributed over $[-\pi, \pi]$ [49, Eq. (7)].

[4]Note that the LMMSE estimator in (22) of the radar sensing channel is reminiscent of LMMSE equalizers in communication systems (e.g., [46, Eq. (2.41)]). Such connections illustrate the underlying synergy between sensing and communications, highlighting how foundational techniques can be adapted to address challenges (see Fig. 2) arising in different fields such as ISAC.

[5]The LMMSE estimator can be applied to any type of waveform, not just OFDM, that results in a linear input-output relationship as in (19), e.g., orthogonal time frequency space (OTFS) [44], [50].

[6]This indicates that the LMMSE estimator can also improve the sensing performance of non-constant-envelope chirp-based waveforms, such as the dual-mode chirp spread spectrum (DM-CSS) waveform [51], when compared to RF and MF estimators.

TABLE I

GUIDELINES ON WHICH ESTIMATOR TO USE IN OFDM RADAR SENSING WITH HIGH-ORDER MODULATIONS UNDER DIFFERENT SNR REGIMES

	RF	MF	LMMSE
Low SNR	✗	✓	✓
High SNR	✓	✗	✓

TABLE II

SIMULATION PARAMETERS

Carrier frequency, f_c	28 GHz
Subcarrier spacing, Δf	120 kHz
Number of subcarriers, N	3330
Bandwidth, B	400 MHz
Number of symbols, M	1120
Transmit power, P_{T}	20 dBm
ULA size at the ISAC TX, N_{T}	8
ULA size at the sensing RX, N_{R}	8
Noise PSD	-174 dBm/Hz

Corollary 2: The RF and MF estimators achieve the highest PSLR with PSK modulation and result in lower PSLR values with QAM modulations.

Proof: Please see Appendix E. ■

Remark 1 (Increasing Side-Lobe Levels With Modulation Order): Corollary 2 establishes a theoretical basis for the increase in side-lobe levels with increasing modulation order in Fig. 2.

Corollary 3: The RF estimator achieves lower side-lobe levels (i.e., higher PSLR) than the MF estimator when the SNR exceeds a certain threshold that depends on the employed modulation. Specifically,

$$\mathrm{PSLR}^{\mathrm{RF}} \geq \mathrm{PSLR}^{\mathrm{MF}} \iff \mathrm{SNR} \geq \frac{\mathbb{E}\left\{\frac{1}{|x|^2}\right\} - 1}{\mathbb{E}\left\{|x|^4\right\} - 1}. \quad (29)$$

Proof: The proof follows readily from (24) and (25). ■

6) Illustrative Example: We provide illustrative examples in Fig. 3 and Fig. 4 to showcase the behavior of the estimators in (15), (16) and (22) with 1024−QAM modulation. The figures demonstrate the range and velocity profiles obtained by 2-D FFT [11], [27], [33], [36] on $\widehat{\mathbf{H}}_{i,b}$ under two different scenarios corresponding to low and high SNR operation[7]. We observe that the proposed LMMSE approach emerges as a robust and globally effective solution, maintaining low side-lobe levels under high-order QAM modulations across all SNR conditions. In contrast, conventional RF and MF estimators struggle with the detection of weak targets due to increased side-lobe levels at low and high SNRs, respectively. These results corroborate Proposition 2 and 3, and Corollary 1. Drawing from these findings, Table I offers general guidelines for selecting estimators to achieve robust sensing performance across various SNR levels.

[7]Defining $\mathrm{SNR}_{\mathrm{mean}} \triangleq \sum_{b=1}^{B} \mathrm{SNR}_b/B$, the low and high SNR scenarios have $\mathrm{SNR}_{\mathrm{mean}} = -29.7$ dB and $\mathrm{SNR}_{\mathrm{mean}} = 19.5$ dB in Fig. 3, and $\mathrm{SNR}_{\mathrm{mean}} = -21.5$ dB and $\mathrm{SNR}_{\mathrm{mean}} = 35.5$ dB in Fig. 4.

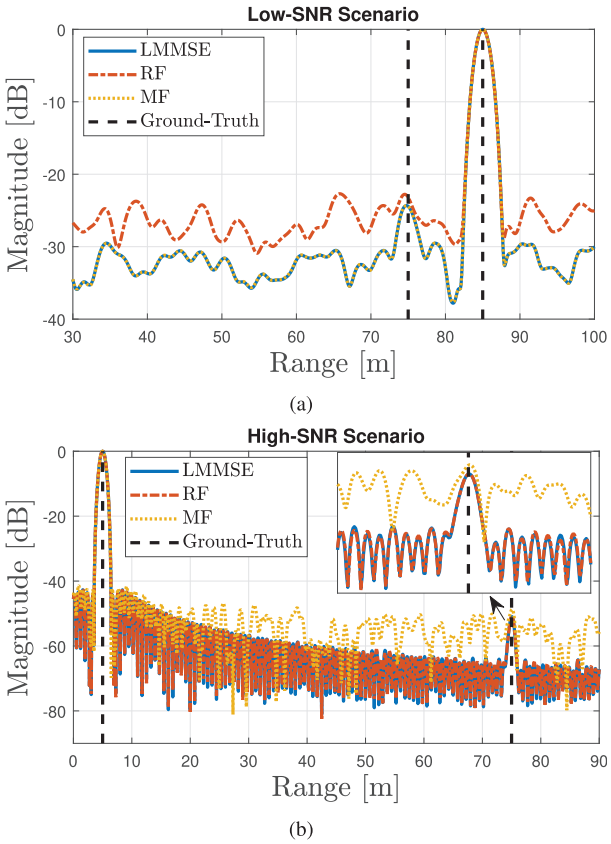

Fig. 3. Comparative analysis of range profiles obtained by different channel estimation strategies with 1024−QAM modulation. (a) Low-SNR scenario with the OFDM parameters in Table II except $B = 100$ MHz and $M = 140$. The scenario involves two targets, each moving at 15 m/s, with RCSs of $(-7, 20)$ dBsm and located at ranges of $(75, 85)$ m and angles of $(10°, 10°)$. (b) High-SNR scenario with the OFDM parameters in Table II except $B = 200$ MHz and $M = 140$. The scenario involves two targets, each moving at 15 m/s, with RCSs of $(15, 20)$ dBsm and located at ranges of $(75, 5)$ m and angles of $(10°, 10°)$. As opposed to the RF and MF estimators, which fail, respectively, at low and high SNRs, the proposed LMMSE approach provides a globally effective solution that achieves low side-lobe levels under high-order QAM modulations across diverse SNR conditions.

B. Beam-Specific Delay-Doppler Estimation

We are now interested in estimating target delays and Dopplers from the output of channel estimation $\widehat{\mathbf{H}}_{i,b}$ in (15), (16) or (22). The channel estimates will have the form

$$\widehat{\mathbf{H}}_{i,b} = \mathbf{H}_{i,b} + \mathbf{Z}_{i,b} \in \mathbb{C}^{N \times M_b}, \quad (30)$$

where $\mathbf{H}_{i,b}$ is given in (12) and $\mathbf{Z}_{i,b}$ represents the channel estimation error term. Based on (12) and following a generalized likelihood ratio test (GLRT) approach [36], the delay-Doppler images can be computed simply via 2-D FFT, i.e.,

$$h_{i,b}(\tau, \nu) = \mathbf{b}^H(\tau) \widehat{\mathbf{H}}_{i,b} \mathbf{c}_b(\nu), \quad (31)$$

where $\mathbf{b}(\tau)$ in (13) and $\mathbf{c}_b(\nu)$ in (14) coincide with (zero-padded) DFT matrix columns. In matrix form with sampled delay-Doppler grid, (31) can be written as

$$\widehat{\mathbf{H}}_{i,b}^{\mathrm{DD}} = \mathbf{F}_N^H \widehat{\mathbf{H}}_{i,b} \mathbf{F}_{M_b} \in \mathbb{C}^{N \times M_b}, \quad (32)$$

where $\mathbf{F}_N \in \mathbb{C}^{N \times N}$ is the unitary DFT matrix of size N. Since target angles are a-priori unknown and 3-D delay-Doppler-angle processing is computationally demanding, we propose

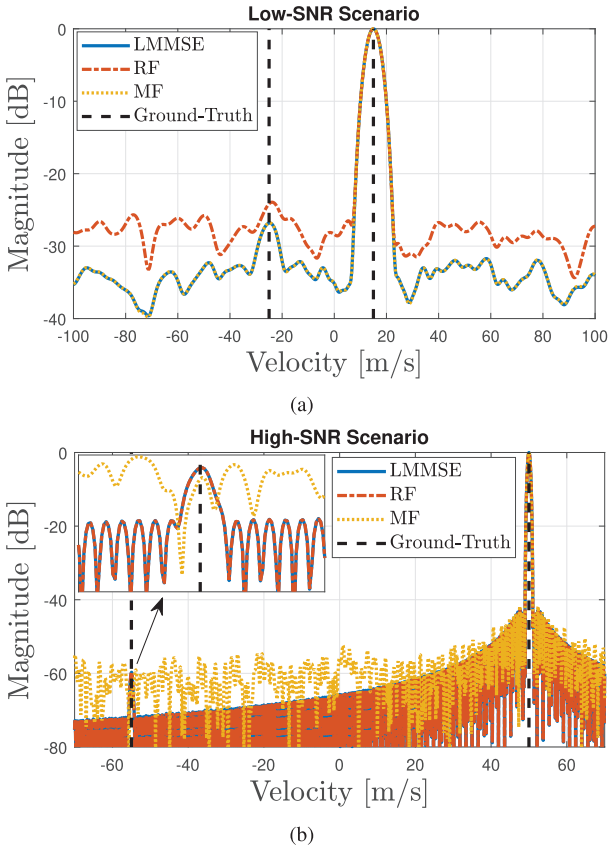

Fig. 4. Comparative analysis of velocity profiles obtained by different channel estimation strategies with 1024−QAM modulation. (a) Low-SNR scenario with the OFDM parameters in Table II except $B = 100\,\mathrm{MHz}$ and $M = 140$. The scenario involves two targets, each located at 75 m and 10°, with RCSs of $(-7, 20)$ dBsm, and moving at $(-25, 15)$ m/s. (b) High-SNR scenario with the OFDM parameters in Table II except $B = 100\,\mathrm{MHz}$ and $M = 1120$. The scenario involves two targets, each located at 5 m and 10°, with RCSs of $(-30, 30)$ dBsm and moving at $(-55, 50)$ m/s.

to non-coherently integrate over the antenna elements [43], [44] to obtain the delay-Doppler image for each beam b (i.e., without seeking phase-alignment with $[\mathbf{a}_{\mathrm{R}}(\theta_k)]_i$ in (12)):

$$\widehat{\mathbf{H}}_b^{\mathrm{DD}} = \sum_{i=1}^{N_{\mathrm{R}}} \left|\widehat{\mathbf{H}}_{i,b}^{\mathrm{DD}}\right|^2 . \tag{33}$$

Multiple target detection and delay-Doppler estimation can be performed by searching for peaks in (33), e.g., via a constant false alarm rate (CFAR) detector [40].

C. Multi-Target Angle Estimation per Delay-Doppler Cell

For each delay-Doppler detection $(\widehat{\tau}, \widehat{\nu})$ obtained via 2-D CFAR on $\widehat{\mathbf{H}}_b^{\mathrm{DD}}$ in (33), we estimate angles of (possibly) multiple targets residing within the resolution cell of $(\widehat{\tau}, \widehat{\nu})$. To this end, we construct the spatial domain compressed observation $\widehat{\mathbf{y}}_b \in \mathbb{C}^{N_{\mathrm{R}}\times 1}$ from the original channel estimates in (30) as follows:

$$\begin{aligned}[\widehat{\mathbf{y}}_b]_i &= \frac{1}{NM_b}\mathbf{b}^H(\widehat{\tau})\widehat{\mathbf{H}}_{i,b}\mathbf{c}_b(\widehat{\nu}) , \\ &= \sum_{k=0}^{K-1} \alpha_{b,k}\frac{\mathbf{b}^H(\widehat{\tau})\mathbf{b}(\tau_k)}{N}\frac{\mathbf{c}_b^H(\nu_k)\mathbf{c}_b(\widehat{\nu})}{M_b}[\mathbf{a}_{\mathrm{R}}(\theta_k)]_i + [\mathbf{n}_b]_i , \\ &\approx \sum_{k\in\mathcal{K}_{(\widehat{\tau},\widehat{\nu})}} \alpha_{b,k}[\mathbf{a}_{\mathrm{R}}(\theta_k)]_i + [\mathbf{n}_b]_i , \end{aligned} \tag{34}$$

where $[\mathbf{n}_b]_i \triangleq \frac{1}{NM_b}\mathbf{b}^H(\widehat{\tau})\mathbf{Z}_{i,b}\mathbf{c}_b(\widehat{\nu})$ is the noise component, $\mathcal{K}_{(\widehat{\tau},\widehat{\nu})} \subseteq \{1,\ldots,K\}$ contains the indices of the targets located within the resolution cell of $(\widehat{\tau}, \widehat{\nu})$ (i.e., $|\mathbf{b}^H(\widehat{\tau})\mathbf{b}(\tau_{k_1})| \gg |\mathbf{b}^H(\widehat{\tau})\mathbf{b}(\tau_{k_2})|$ and $|\mathbf{c}_b^H(\widehat{\nu})\mathbf{c}_b(\nu_{k_1})| \gg |\mathbf{c}_b^H(\widehat{\nu})\mathbf{c}_b(\nu_{k_2})|$ for $k_1 \in \mathcal{K}_{(\widehat{\tau},\widehat{\nu})}, k_2 \notin \mathcal{K}_{(\widehat{\tau},\widehat{\nu})}$). Stacking (34) over the RX array yields

$$\widehat{\mathbf{y}}_b = \sum_{k\in\mathcal{K}_{(\widehat{\tau},\widehat{\nu})}} \alpha_{b,k}\mathbf{a}_{\mathrm{R}}(\theta_k) + \mathbf{n}_b . \tag{35}$$

Due to relatively small number of antenna elements N_{R} at typical ISAC sensing receivers, we propose to retrieve multiple angles from (35) using the ESPRIT algorithm in order to resolve targets closely spaced in the angular domain. In particular, we resort to 1-D ESPRIT using spatial smoothing with Hankel matrix construction [53], [54]. Due to space limitations, the reader is referred to [53, Sec. IV-D]and [54, Sec. III-A] for details on multiple angle estimation using (35).

D. Beam-Specific Gain Estimation

Given the estimates $\mathcal{E}_b = \{\widehat{\tau}_{b,k}, \widehat{\nu}_{b,k}, \widehat{\theta}_{b,k}\}_{k=1}^{K_b}$ from the beam-specific processing for the b^{th} beam, we estimate the corresponding target gains $\boldsymbol{\alpha}_b \in \mathbb{C}^{K_b\times 1}$ via least-squares (LS) using the channel estimates $\{\widehat{\mathbf{H}}_{i,b}\}_{i=1}^{N_{\mathrm{R}}}$ in (30). Based on the channel structure in (30) and (12), the channel estimates over all RX antenna elements can be expressed as

$$\widehat{\mathbf{h}}_b \triangleq \begin{bmatrix}\widehat{\mathbf{h}}_{1,b}\\ \vdots \\ \widehat{\mathbf{h}}_{N_{\mathrm{R}},b}\end{bmatrix} = \underbrace{\begin{bmatrix}\mathbf{A}_{1,b}\\ \vdots \\ \mathbf{A}_{N_{\mathrm{R}},b}\end{bmatrix}}_{\triangleq\mathbf{A}_b\in\mathbb{C}^{NM_bN_{\mathrm{R}}\times K_b}} \boldsymbol{\alpha}_b + \mathbf{z}_b , \tag{36}$$

where $\widehat{\mathbf{h}}_{i,b} \triangleq \mathrm{vec}\big(\widehat{\mathbf{H}}_{i,b}\big) \in \mathbb{C}^{NM_b\times 1}$, $\mathbf{A}_{i,b} \triangleq [\mathbf{a}_{i,b}^{(1)} \ \ldots \ \mathbf{a}_{i,b}^{(K_b)}] \in \mathbb{C}^{NM_b\times K_b}$ „ and $\mathbf{a}_{i,b}^{(k)} \triangleq [\mathbf{a}_{\mathrm{R}}(\widehat{\theta}_{b,k})]_i\, \mathbf{c}_b^*(\widehat{\nu}_{b,k}) \otimes \mathbf{b}(\widehat{\tau}_{b,k}) \in \mathbb{C}^{NM_b\times 1}$. Using (36), the gain estimates can be obtained as

$$\widehat{\boldsymbol{\alpha}}_b = \mathbf{A}_b^{\dagger}\widehat{\mathbf{h}}_b . \tag{37}$$

Algorithm 1 Beam-Specific Parameter Estimation From Unstructured Radar Channel Estimates

1: **Input:** Frequency/slow-time radar channel estimates $\{\widehat{\mathbf{H}}_{i,b}\}_{i=1}^{N_{\mathrm{R}}}$ for the b^{th} beam in (15), (16) or (22), probability of false alarm P_{fa}.
2: **Output:** Delay, Doppler, angle and gain estimates $\{\widehat{\tau}_{b,k}, \widehat{\nu}_{b,k}, \widehat{\theta}_{b,k}, \widehat{\alpha}_{b,k}\}_{k=1}^{K_b}$ of multiple targets.
3: Obtain the noncoherentlyintegrated delay-Dopplerimage $\widehat{\mathbf{H}}_b^{\mathrm{DD}}$ for the b^{th} beam via (32) and (33).
4: Run a CFAR detector on $\widehat{\mathbf{H}}_b^{\mathrm{DD}}$ with the specified P_{fa} for target detection in the delay-Doppler domain.
5: For each delay-Doppler detection $(\widehat{\tau}, \widehat{\nu})$, compute the spatial domain observation $\widehat{\mathbf{y}}_b$in (34).
6: Estimate angles from $\widehat{\mathbf{y}}_b$ via 1-D ESPRIT.
7: Using the estimates $\{\widehat{\mathbf{H}}_{i,b}\}_{i=1}^{N_{\mathrm{R}}}$ and $\{\widehat{\tau}_{b,k}, \widehat{\nu}_{b,k}, \widehat{\theta}_{b,k}\}_{k=1}^{K_b}$, estimate the gains via (36)–(37).

Algorithm 2 LMMSE-Based MIMO-OFDM Radar Sensing

1: **Input:** Space/frequency/slow-time MIMO-OFDM radar data cube $\{\mathbf{y}_{n,m}\}$ in (5), transmit symbols $\mathbf{X}$, number of distinct beams B, probability of false alarm P_{fa}.
2: **Output:** Delay-Doppler-angle estimates $\{\widehat{\tau}_k, \widehat{\nu}_k, \widehat{\theta}_k\}_{k=0}^{K-1}$ of multiple targets.
3: **for** $b = 1, \ldots, B$
4: Compute the RF, MF and LMMSE channel estimate $\widehat{\mathbf{H}}_{i,b}$ in (15), (16) and (22), respectively, for each RX element $i = 1, \ldots, N_{\text{R}}$ using $\text{SNR}_b = 1$ in (22).
5: For each estimate, run Algorithm 1 to obtain the estimates $\mathcal{E}_b = \{\widehat{\tau}_{b,k}, \widehat{\nu}_{b,k}, \widehat{\theta}_{b,k}, \widehat{\alpha}_{b,k}\}_{k=1}^{K_b}$ and compute the corresponding SNRs via (37) and (38).
6: Compute two LMMSE channel estimates in (22) with thetwo SNRs obtained using the RF and MF estimates and run Algorithm 1.
7: Merge the detections from the three LMMSE estimatorsand cluster them via DBSCAN in Sec. III-F.
8: Compute the resulting SNR_b via (37) and (38), and the corresponding LMMSE channel estimate in (22) by inserting SNR_b and run Algorithm 1.
9: **end for**
10: Perform DBSCAN clustering of the resulting detections $\{\mathcal{E}_b\}_{b=1}^{B}$ using the settings in Sec. III-F.

E. LMMSE Processing With A-Priori Unknown Gains

The LMMSE estimator expression in (22) involves the SNR term SNR_b, the evaluation of which requires the knowledge of the target channel gains (i.e., $\sigma^2_{\alpha_{b,k}} = \mathbb{E}\{|\alpha_{b,k}|^2\}$). Since the channel gains are a-priori unknown, we propose to first run the LMMSE estimator in (22) using three different SNR_b values, following the subsequent processing steps in Sec. III-B–Sec. III-C, and merge and cluster the detections obtained via the different SNR_b values (see Lines 4– 7 of Algorithm 2). Then, we plug the resulting gain estimates from (37) into the SNR expression (22), i.e.,

$$\text{SNR}_b = \|\widehat{\boldsymbol{\alpha}}_b\|^2 / \sigma^2 , \tag{38}$$

which can now be inserted into (22) for LMMSE estimation.

F. Clustering Detections Over All Beams

Since the same target might be detected in multiple beams during beam sweeping, we need a clustering algorithm to merge detections from all beams. To this end, given the estimates $\{\mathcal{E}_b\}_{b=1}^{B}$, we resort to the density-based spatial clustering of applications with noise (DBSCAN) algorithm [55], [56] to cluster detections over B beams. In DBSCAN, we set the minimum number of points in a cluster to 1 and define the distance measure (used to characterize the ϵ-neighbourhood of a point [55]) in the range-velocity-angle space as the weighted Euclidean distance:

$$d_{\mathbf{W}}(\widehat{\mathbf{s}}_p, \widehat{\mathbf{s}}_q) = [(\widehat{\mathbf{s}}_p - \widehat{\mathbf{s}}_q)^T \mathbf{W} (\widehat{\mathbf{s}}_p - \widehat{\mathbf{s}}_q)]^{1/2} , \tag{39}$$

where $\widehat{\mathbf{s}}_p = [\widehat{R}_p, \widehat{v}_p, \widehat{\theta}_p]^T$ contains the range, velocity and angle estimates of the p^{th} detection in $\{\mathcal{E}_b\}_{b=1}^{B}$, and $\mathbf{W} \in \mathbb{R}^{3\times 3}$ is a diagonal matrix to account for scaling due to unit differences. The ϵ parameter [55] is set to $\epsilon = (\mathbf{s}_\Delta^T \mathbf{W} \mathbf{s}_\Delta)^{1/2}$, where $\mathbf{s}_\Delta = [\Delta R, \Delta v, \Delta\theta]^T$ with $\Delta R = c/(2N\Delta f)$ denoting the range resolution, $\Delta v = \lambda B/(2MT_{\text{sym}})$ the velocity resolution per beam and[8] $\Delta\theta = 2^\circ$.

G. Summary of the Proposed Algorithm

The proposed LMMSE based sensing algorithm is summarized in Algorithm 2, which uses Algorithm 1 as a subroutine.

IV. Communications Data Rate Evaluation

In this section, we provide a methodology to evaluate the data rate of the communications subsystem of the considered ISAC system under different constellations, extending [14] to the case with imperfect channel state information (CSI).

A. Calculation of Mutual Information

The received signal at the communications RX in (9) can be recast as $y^{\text{com}}_{n,m} = h_{n,m} x_{n,m} + z_{n,m}$, where $h_{n,m} \triangleq (\mathbf{h}^{\text{com}}_{n,m})^T \mathbf{f}_m$. As we accumulate the values of $y^{\text{com}}_{n,m}$ over the entire OFDM frame, we obtain

$$\mathbf{Y}^{\text{com}} = \mathbf{H} \odot \mathbf{X} + \mathbf{Z} , \tag{40}$$

where $\mathbf{Y}^{\text{com}} \in \mathbb{C}^{N\times M}$ with $[\mathbf{Y}^{\text{com}}]_{n,m} = y^{\text{com}}_{n,m}$, the effective channel matrix $\mathbf{H} \in \mathbb{C}^{N\times M}$ with $[\mathbf{H}]_{n,m} = h_{n,m}$, and $\mathbf{Z} \in \mathbb{C}^{N\times M}$ is a noise matrix with independently and identically distributed (i.i.d.) entries $z_{n,m} \sim \mathcal{CN}(0, \sigma_{\text{c}}^2)$. Hence, the mutual information (MI) of the entire frame can be written as

$$\mathcal{I}(\mathbf{X}; \mathbf{Y}^{\text{com}} | \mathbf{H}) = \sum_{n,m} \mathcal{I}(x_{n,m}; y^{\text{com}}_{n,m}) . \tag{41}$$

The separability of the MI in (41) results from the independence of $y^{\text{com}}_{n,m}$ across subcarriers and symbols.

To declutter the notation, we drop the indices and consider the received signal as $y = hx + z$, where h is the deterministic channel, x is the transmit symbol uniformly distributed over a finite alphabet $\mathcal{X} = \{x_1, x_2, \ldots, x_L\}$ and $z \sim \mathcal{CN}(0, \sigma_{\text{c}}^2)$. Under imperfect CSI, h can be expressed as [57]

$$h = \overline{h} + \varepsilon , \tag{42}$$

where $\overline{h}$ is the random channel estimate and $\varepsilon \sim \mathcal{CN}(0, \sigma_{\text{e}}^2)$ denotes the estimation error, leading to

$$y = \overline{h} x + \varepsilon x + z . \tag{43}$$

In (43), the MI between x and y can be written as [57]

$$\begin{aligned} \mathcal{I}(x; y) &= \mathbb{E}_{\widehat{h}}[\mathcal{I}(x; y \,|\, \overline{h} = \widehat{h})] , \\ &= \mathbb{E}_{\widehat{h}}[\mathcal{H}(y \,|\, \overline{h} = \widehat{h})] - \mathbb{E}_{\widehat{h}}[\mathcal{H}(y \,|\, x, \overline{h} = \widehat{h})] , \end{aligned} \tag{44}$$

where $\mathcal{H}(y \,|\, \overline{h} = \widehat{h})$ and $\mathcal{H}(y \,|\, x, \overline{h} = \widehat{h})$ denote the conditional entropy of y and $y \,|\, x$, respectively, given $\overline{h} = \widehat{h}$. Summing (44) over subcarriers and symbols yields the MI in (41).

[8] Since the ESPRIT algorithm in Sec. III-C offers higher angular resolution than the standard Rayleigh resolution of $\mathbf{a}_{\text{R}}(\theta)$ in (8), we set the proximity criterion in angle to a lower value than the standard resolution.

B. Evaluation of Entropies in (44)

We now evaluate the second term in the entropy expression in (44). From (43), we have

$$y \,|\, x = x_\ell, \overline{h} = \widehat{h} \sim \mathcal{CN}\left(\widehat{h}x_\ell, |x_\ell|^2\sigma_{\mathrm{e}}^2 + \sigma_{\mathrm{c}}^2\right), \tag{45}$$

leading to [58]

$$\mathcal{H}(y \,|\, x, \overline{h} = \widehat{h}) = \frac{1}{L}\sum_{\ell=1}^{L} \log_2\left(\pi e(|x_\ell|^2\sigma_{\mathrm{e}}^2 + \sigma_{\mathrm{c}}^2)\right). \tag{46}$$

Since (46) is independent of $\widehat{h}$, the second term in (44) is directly given by (46).

The argument inside the expectation in the first term in (44) can be expressed as

$$\begin{aligned}\mathcal{H}(y \,|\, \overline{h} = \widehat{h}) &= \mathbb{E}_{y \,|\, \overline{h}=\widehat{h}}\left[-\log_2 f(y \,|\, \overline{h} = \widehat{h})\right], \\ &\approx -\frac{1}{N_{\mathrm{s}}}\sum_{i=1}^{N_{\mathrm{s}}} \log_2 f(y_i \,|\, \overline{h} = \widehat{h}),\end{aligned} \tag{47}$$

where N_{s} denotes the number of samples drawn from $\mathcal{X}$. The approximation herein leverages the law of large numbers and becomes exact as N_{s} increases. For the i^{th} sample, we draw a symbol $x_{\ell(i)}$ (where $\ell(i) \in \{1, \ldots, L\}$) from $\mathcal{X}$ and generate a realization of $z \sim \mathcal{CN}(0, \sigma_{\mathrm{c}}^2)$ to compute a realization of the received signal as $y_i = hx_{\ell(i)} + z_i$. For a given $\overline{h} = \widehat{h}$, (47) can be evaluated using (45) in the same manner as in (46):

$$\begin{aligned}&f(y_i \,|\, \overline{h} = \widehat{h}) \\ &= \frac{1}{L}\sum_{\ell=1}^{L} f(y_i \,|\, \overline{h} = \widehat{h}, x_\ell), \\ &= \sum_{\ell=1}^{L} \frac{1}{L\pi(|x_\ell|^2\sigma_{\mathrm{e}}^2 + \sigma_{\mathrm{c}}^2)} \exp\left(-\frac{|y_i - \widehat{h}x_\ell|^2}{|x_\ell|^2\sigma_{\mathrm{e}}^2 + \sigma_{\mathrm{c}}^2}\right).\end{aligned} \tag{48}$$

We can now evaluate the first term in (44) by inserting (47) and (48), and taking expectation over the distribution of $\widehat{h}$:

$$\begin{aligned}&\mathbb{E}_{\widehat{h}}[\mathcal{H}(y \,|\, \overline{h} = \widehat{h})] \\ &\approx \log_2(L\pi) \\ &\quad - \frac{1}{N_{\mathrm{s}}}\sum_{i=1}^{N_{\mathrm{s}}} \mathbb{E}_{\widehat{h}}\left[\log_2\left(\sum_{\ell=1}^{L} \kappa_\ell \exp\left(-\kappa_\ell |y_i - \widehat{h}x_\ell|^2\right)\right)\right],\end{aligned} \tag{49}$$

where $\kappa_\ell \triangleq \frac{1}{|x_\ell|^2\sigma_{\mathrm{e}}^2 + \sigma_{\mathrm{c}}^2}$. Using a similar Monte Carlo sampling approach as in (47), one can evaluate the expectation in (49) by drawing N_{h} samples from $\widehat{h} \sim \mathcal{CN}(h, \sigma_{\mathrm{e}}^2)$ (see (42)):

$$\begin{aligned}&\mathbb{E}_{\widehat{h}}\left[\log_2\left(\sum_{\ell=1}^{L} \kappa_\ell \exp\left(-\kappa_\ell |y_i - \widehat{h}x_\ell|^2\right)\right)\right] \\ &\approx \frac{1}{N_{\mathrm{h}}}\sum_{j=1}^{N_{\mathrm{h}}} \log_2\left(\sum_{\ell=1}^{L} \kappa_\ell \exp\left(-\kappa_\ell |y_i - \widehat{h}_j x_\ell|^2\right)\right).\end{aligned} \tag{50}$$

We now insert (50) into (49) to obtain

$$\mathbb{E}_{\widehat{h}}[\mathcal{H}(y \,|\, \overline{h} = \widehat{h})] \approx \log_2(L\pi) - \frac{1}{N_{\mathrm{s}}N_{\mathrm{h}}}\sum_{i=1}^{N_{\mathrm{s}}}\sum_{j=1}^{N_{\mathrm{h}}} g(y_i, \widehat{h}_j), \tag{51}$$

where $g(y_i, \widehat{h}_j) \triangleq \log_2\left(\sum_{\ell=1}^{L} \kappa_\ell \exp\left(-\kappa_\ell |y_i - \widehat{h}_j x_\ell|^2\right)\right)$.

Algorithm 3 Rate Evaluation Under Different Constellations

Input: Frequency/slow-time communication channel $\mathbf{H}$ in (40), alphabet $\mathcal{X} = \{x_1, x_2, \ldots, x_L\}$, number of samples for entropy approximation N_{s}, N_{h}.
Output: MI in (41).
for $n = 0, \ldots, N-1$, $m = 0, \ldots, M-1$ **do**
  for $j = 1, \ldots, N_{\mathrm{h}}$ **do**
    Generate a realization of channel estimate, $\widehat{h}_{n,m}^{j}$, from $\mathcal{CN}(h_{n,m}, \sigma_{\mathrm{e}}^2)$.
    for $i = 1, \ldots, N_{\mathrm{s}}$ **do**
      Select a symbol $x_{\ell(i)}$(where $\ell(i) \in \{1, \ldots, L\}$) from $\mathcal{X}$ in a uniformly random manner.
      Generate a noise realization z_i from $\mathcal{CN}(0, \sigma_{\mathrm{c}}^2)$.
      Calculate the output via $y_i = h_{n,m}x_{\ell(i)} + z_i$.
      Compute $g(y_i, \widehat{h}_{n,m}^{j})$ in (51).
    end for
  end for
  Compute $\mathbb{E}_{\widehat{h}}[\mathcal{H}(y \,|\, \overline{h} = \widehat{h})]$ via (51).
  Compute $\mathbb{E}_{\widehat{h}}[\mathcal{H}(y \,|\, x, \overline{h} = \widehat{h})]$ via (46).
  Compute the MI in (44) via (46) and (51).
end for
Compute the MI of the entireframe in (41) by summing (44) over N subcarriers and M symbols.

C. General Procedure to Evaluate MI in (41)

Drawing from Sec. IV-A and Sec. IV-B, we outline the MI evaluation process from (41) in Algorithm 3.

V. Simulation and Experimental Results

In this section, we assess the performance of the proposed sensing algorithm in Algorithm 2 as well as the accompanying ISAC trade-offs using the data rate evaluation procedure in Algorithm 3 on both simulated and experimentally obtained data. The default simulation parameters are provided in Table II. For sensing beam sweeping in Sec. II-E, we set the number of beams $B = N_{\mathrm{T}}$ and $\theta_{\max} = 70°$. To evaluate the detection performance, we set $P_{\mathrm{fa}} = 10^{-4}$ in Algorithm 2 and consider 100 independent Monte Carlo noise realizations in (5), where each realization corresponds to a 3-D noise tensor of size $N_{\mathrm{R}}NM$. Unless otherwise stated, we set $\sigma_{\mathrm{e}}^2 = 0$ in Algorithm 3, i.e., perfect CSI. For benchmarking purposes, we compare the ISAC performance of the following algorithms:

- **LMMSE**: The proposed MIMO-OFDM radar sensing algorithm in Algorithm 2.
- **LMMSE (ideal)**: The genie-aided version of Algorithm 2 where the true value of SNR_b is inserted into (22) on Line 8 by skipping Lines 4– 7. This serves as an upper bound on the performance of LMMSE.
- **RF**: The standard RF-based sensing algorithm that executes Algorithm 2 by skipping Lines 6– 8.
- **MF**: The standard MF-based sensing algorithm that executes Algorithm 2 by skipping Lines 6– 8.
- **RF-SOTA**: The state-of-the-art RF-based MIMO-OFDM radar sensing algorithm in [6].

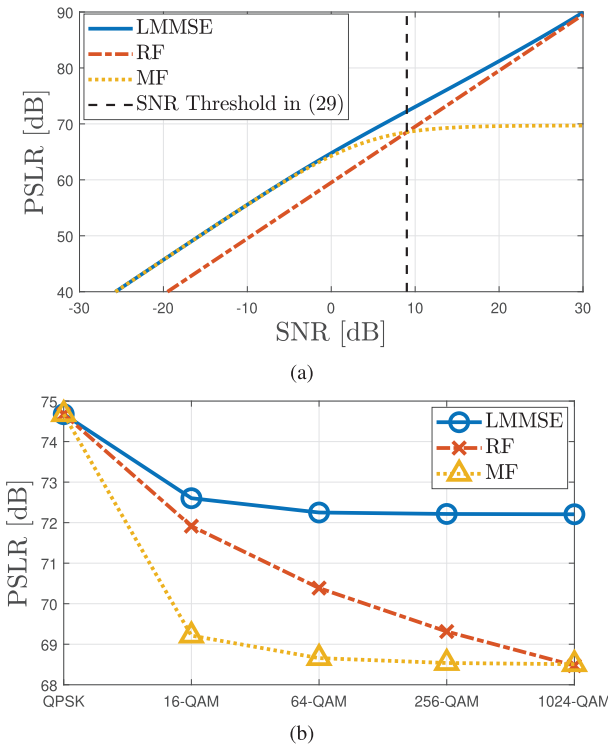

Fig. 5. PSLR in (23) for different OFDM radar receivers with respect to: (a) SNR using 1024−QAM modulation, along with the RF-MF SNR threshold in (29), and (b) modulation order at SNR = 9 dB.

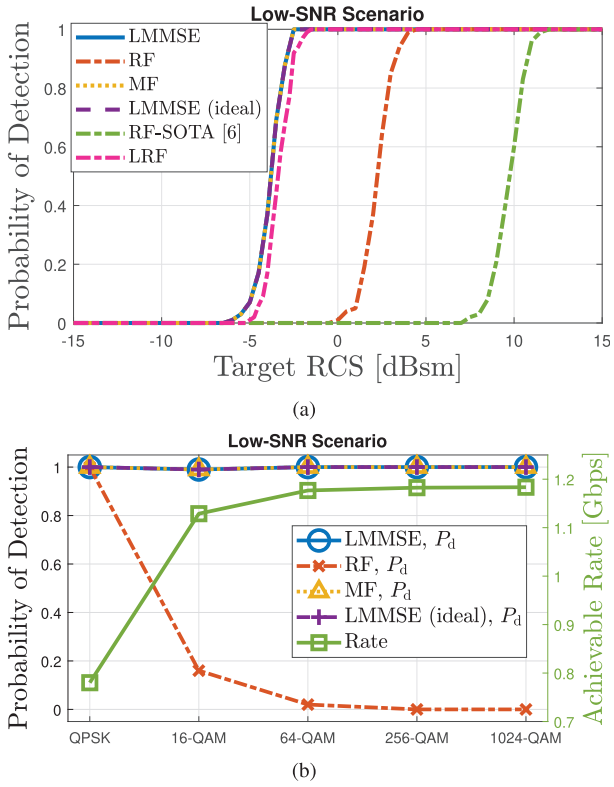

Fig. 6. ISAC performances in the low-SNR sensing scenario under concurrent transmission. (a) Probability of detection with respect to target RCS using 1024−QAM data. (b) Probability of detection and achievable rate with respect to modulation order for target RCS of −2 dBsm.

- **LRF**: Loaded reciprocal filter (LRF) in [47], given by $\widehat{\mathbf{H}}_{i,b} = \frac{\mathbf{Y}_{i,b} \odot e^{-j\angle \mathbf{X}_b}}{\sqrt{|\mathbf{X}_b|^2 + \gamma_{\text{LRF}}}}$, with a loading constant[9] γ_{LRF}.

For the communication channel in (10), we consider the presence of $\widetilde{K} = 4$ paths to an RX located at $[43, -25]^T$ m with respect to the ISAC TX, including a LOS path and 3 non-line-of-sight (NLOS) paths. The corresponding scatterers are located at $[40, -20]^T$ m, $[42, -27]^T$ m and $[38, -30]^T$ m, with the RCSs $\{-5, -10, -10\}$ dBsm, respectively. Considering stationary RX and scatterers, we set $\widetilde{\nu}_k = 0$ for all the paths.

In the following subsections, we first analyze the PSLR expressions given in Sec. III-A5, followed by an investigation of the time-frequency and spatial domain ISAC trade-offs under concurrent transmission. Then, we compare concurrent and time-sharing strategies as described in Sec. II-B. Finally, we provide experimental results using real-world OFDM monostatic sensing measurements to verify the behaviour of the considered algorithms as illustrated in Fig. 2 and Fig. 3.

A. PSLR Analysis

To demonstrate the analytical PSLR expressions in Proposition 1 for various modulations and OFDM radar receivers, and to confirm the theoretical insights from Proposition 2 and 3, and Corollaries 1–3, we present in Fig. 5 the PSLR levels obtained by LMMSE, RF and MF against SNR (for 1024−QAM modulation) and modulation order (at a fixed SNR of 9 dB), using parameters from Table II. As shown in Fig. 5(a), LMMSE consistently outperforms MF and RF in PSLR performance across the entire SNR range, converging to MF at low SNRs and RF at high SNRs. This result confirms Proposition 2 and 3, and Corollary 1, and aligns closely with the illustrative examples in Figs. 3 and 4. Fig. 5(a) also verifies the SNR threshold for the RF-MF PSLR transition derived in Corollary 3. From Fig. 5(b), we observe that RF and MF achieve peak PSLR with QPSK modulation and exhibit declining PSLR with higher-order modulations, substantiating Corollary 2. Furthermore, LMMSE attains higher PSLR than RF and MF across all QAM modulations, which, together with Fig. 5(a), indicates its superiority in radar detection (which will be verified in the subsequent sections).

B. Time-Frequency Trade-Offs Under Concurrent Transmission

To investigate time-frequency domain ISAC trade-offs, the performance of the algorithms under concurrent transmission, as outlined in Sec. II-B1, is evaluated using different modulation orders for transmit symbols $\mathbf{X}$ in (5). We set $\rho = 0.8$ in (3) and consider two sensing scenarios, *low-SNR* and *high-SNR* (quantified by SNR_{mean} defined in Footnote 7), which are crucial for highlighting the distinct characteristics of the algorithms, as extensively demonstrated earlier in Fig. 3.

1) Low-SNR Sensing Scenario: In the low-SNR scenario, we consider a single target with range 80 m, velocity 15 m/s, angle 10° and RCS −2 dBsm, leading to $\text{SNR}_{\text{mean}} = -50.6$ dB. The goal is to investigate whether the target is drowned out by its own interference under high-order modulations due to increased side-lobe levels as depicted in

[9] $\gamma_{\text{LRF}} = tN\mathbb{E}\{|x|^2\}$ where we set $t = 0.5$ [47, Eq. (26)].

Fig. 2 and Fig. 3. In Fig. 6(a), we show the probability of detection (P_{d}) of various algorithms relative to target RCS, employing 1024−QAM modulation for $\mathbf{X}$. It is observed that the proposed LMMSE estimator significantly outperforms the RF estimator, achieving gains in P_{d} as high as 1 for a constant RCS and enabling the detection of targets with RCS values smaller by up to 6 dBsm for a specified P_{d}. Furthermore, consistent with the discussions in Sec. III-A4 and findings in Fig. 3(a), LMMSE and MF achieve the same performances. Thus, in compliance with Table I and Fig. 5(a), LMMSE and MF are suitable for low-SNR sensing, whereas RF leads to severe degradations in probability of detection. Moreover, LMMSE matches the detection performance of its genie-aided version, which assumes perfect knowledge of SNR_b in (22), validating the effectiveness of the SNR estimation approach in Algorithm 2. We also observe that LRF outperforms RF, but performs slightly worse than MF due to the noise amplification effect at low SNRs for LRF, arising from the division by $\sqrt{|\mathbf{X}_b|^2+\gamma_{\mathrm{LRF}}}$. Finally, when comparing our proposed MIMO-OFDM radar sensing approach to the state-of-the-art, the RF method in Algorithm 2 substantially outperforms the one in [6]. Indeed, the latter method is more suitable in a tracking scenario where, if the target angular sector is known, the TX and RX beams can be steered towards the target, thereby exploiting receive combining gain. Conversely, in the considered scanning/search scenario where the target angular sector is unknown, the method in [6] fails to fully exploit the available measurements at RX antennas, as reflected in the RCS loss shown in Fig. 6(a).

To investigate ISAC trade-offs, we explore the impact of modulation order on the sensing and communication performances. To this end, in Fig. 6(b) we depict the probability of detection and achievable rate across various modulations, from QPSK to 1024−QAM, for a constant RCS of -2 dBsm. The detection curves reveal the robustness of the proposed LMMSE approach against increasing modulation order, showcasing its capability to mitigate target masking effects under high-order modulations. Conversely, the RF estimator suffers from substantial loss in probability of detection with increasing modulation order due to rising side-lobe levels, corroborating the findings in Fig. 2. Furthermore, the achievable rate improves as modulation order increases, as expected, which suggests that LMMSE (along with its genie-aided, ideal version and MF) achieves much more favorable ISAC trade-offs compared to RF. Hence, employing LMMSE in the sensing receiver enables significant improvements in communication rates through high-order QAM signaling without compromising detection performance.

2) High-SNR Sensing Scenario: We now turn our attention to a high-SNR scenario which contains three targets with ranges of $(75, 5, 5)$ m, velocities of $(15, -10, -10)$ m/s, angles of $(10°, 10°, 18°)$ and RCSs of $(5, 20, 5)$ dBsm, resulting in $\mathrm{SNR}_{\mathrm{mean}} = 19.6$ dB. In Fig. 7(a), we show the probability of detection of Target-1 relative to its RCS with 1024−QAM modulation. It is seen that the proposed LMMSE estimator outperforms RF, MF and LRF benchmarks, indicating that it can effectively reduce side-lobe levels to prevent target masking when using varying-amplitude data.

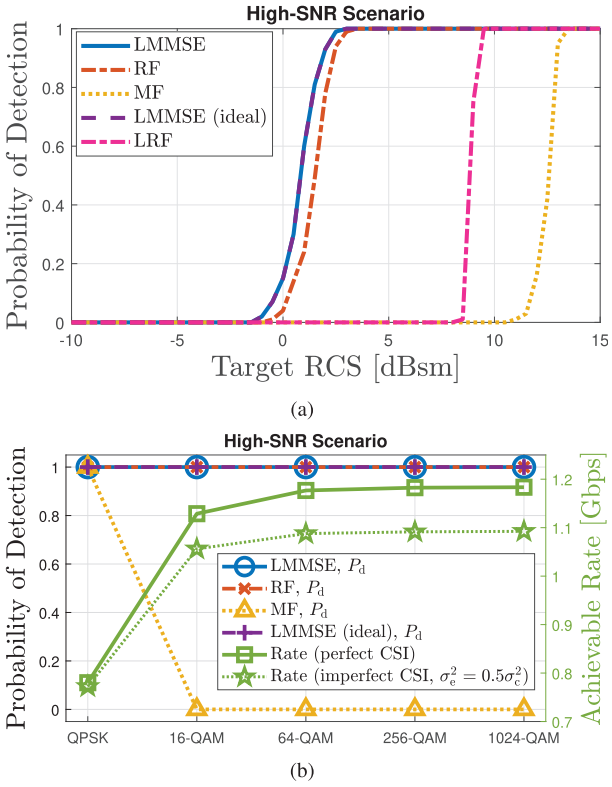

Fig. 7. ISAC performances in the high-SNR sensing scenario under concurrent transmission. (a) Probability of detection with respect to RCS of Target-1 using 1024−QAM data. (b) Probability of detection and achievable rate with respect to modulation order for Target-1 RCS of 5 dBsm.

In particular, LMMSE provides up to 11 dBsm gain in RCS for fixed P_{d} over MF. In accordance with Table I, Fig. 3(b) and Fig. 5(a), at high sensing SNRs, MF experiences significant loss in detection performance, while RF leads to slight degradations in performance compared to LMMSE. We also note that LRF outperforms MF but suffers a considerable performance loss compared to RF. At high SNRs, the impact of varying-amplitude data for LRF is less severe than for MF due to the inclusion of γ_{LRF} in the denominator, which offers an additional degree of freedom to control the side-lobe behavior [47]. However, since γ_{LRF} is not adapted based on SNR, it fails to provide a universally effective solution, unlike LMMSE, which surpasses LRF in both low and high SNR conditions. Moreover, in Fig. 7b we report the probability of detection of Target-1 and achievable rate against modulation order for a fixed Target-1 RCS of 5 dBsm. We observe that MF fails to detect the target when employing 16-QAM modulation and higher, while LMMSE maintains a constant P_{d} of 1 across all modulation orders. The achievable rate under imperfect CSI with $\sigma_{\mathrm{e}}^2 = 0.5\sigma_{\mathrm{c}}^2$ (see (42) and (43)) is also reported, showing reduced rates under channel estimation errors, as expected.

3) Summary of Low-SNR and High-SNR Scenarios: Fig. 6 and Fig. 7 reveal that LMMSE provides consistently superior detection performance across different SNR regimes over existing benchmarks when using high-order QAM signaling. This establishes LMMSE as a universally effective strategy for OFDM radar sensing across a spectrum of SNR levels and modulation schemes, validating the PSLR analysis in Fig. 5.

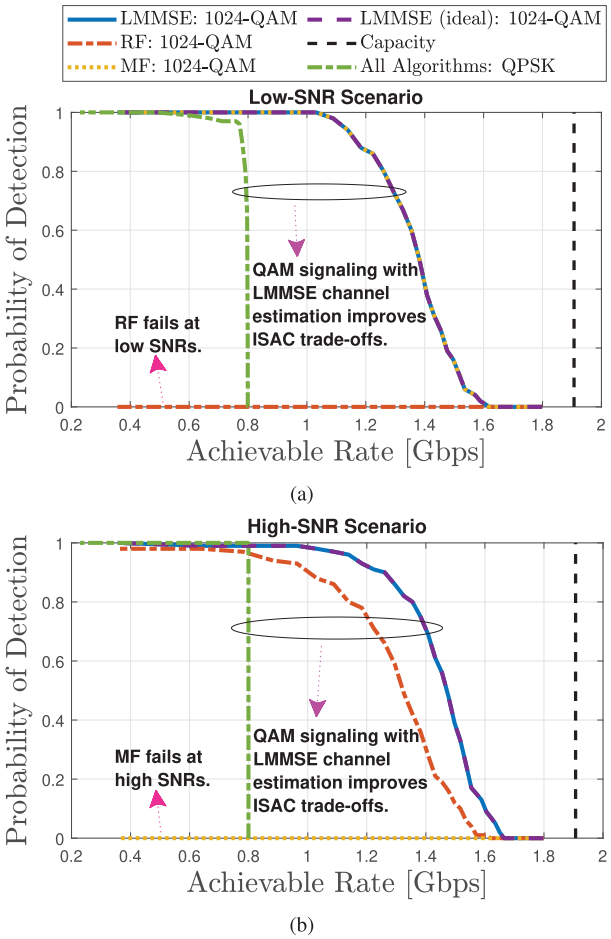

Fig. 8. ISAC trade-off curves under concurrent transmission for QPSK and 1024−QAM modulations as the trade-off weight ρ in (3) varies over $[0, 1]$. (a) Low-SNR sensing scenario for target RCS of -3 dBsm. (b) High-SNR sensing scenario for Target-1 RCS of 2 dBsm.

C. Spatial Trade-Offs Under Concurrent Transmission

To evaluate spatial domain ISAC trade-offs, we study the impact of the trade-off weight ρ in (3) on sensing and communication performances with varying modulation orders for $\mathbf{X}$, considering the same low-SNR and high-SNR scenarios as in Sec. V-B. The low-SNR scenario yields $\text{SNR}_{\text{mean}} = (-60.3, -49.9)$ dB for $\rho = (0, 1)$, respectively, while the high-SNR scenario leads to $\text{SNR}_{\text{mean}} = (9.9, 20.3)$ dB for $\rho = (0, 1)$. In the considered setting, the UE is located at an angle of $-30.2°$, while the targets lie at $10°$ and $18°$. Hence, we expect to observe a trade-off between sensing and communications as ρ varies. In Fig. 8, we plot the ISAC trade-off curves obtained by the algorithms under consideration in the low-SNR and high-SNR scenarios as ρ sweeps the interval $[0, 1]$, using both QPSK and 1024−QAM modulations.[10]

1) Low-SNR Sensing Scenario: Looking at the low-SNR results in Fig. 8(a), LMMSE significantly improves ISAC trade-offs over RF when utilizing 1024−QAM signaling, aligning with insights from Table I and Fig. 6(a). In addition, as expected, the performance of LMMSE mirrors that of MF in low-SNR environments. When comparing QAM and QPSK signaling, we observe that LMMSE can achieve substantially better ISAC trade-offs with QAM signaling through its robustness in detection performance against increasing modulation order (as illustrated in Fig. 6(b)). This robustness enables the use of high-order QAM to boost rates without sacrificing sensing performance.[11]

2) High-SNR Sensing Scenario: As observed in Secs. V-A and V-B, the trends for MF and RF become opposite when transitioning from low-SNR to high-SNR scenarios. Specifically, in high-SNR environments, MF fails to provide satisfactory ISAC trade-off performance whereas RF surpasses MF, albeit with a performance gap compared to LMMSE. Hence, employing QAM signaling at the transmit side, in conjunction with the LMMSE algorithm at the sensing receiver, yields superior ISAC trade-offs over both RF and MF benchmarks.

3) Summary of Low-SNR and High-SNR Scenarios: In alignment with Table I and the previous findings in Fig. 6 and Fig. 7, the spatial domain trade-off results in Fig. 8 demonstrate that LMMSE consistently outperforms the traditional OFDM radar sensing benchmarks MF and RF across various SNRs, modulation schemes and sensing-communication beamforming weights. Based on the findings in Fig. 8, Table III provides rough guidelines on the choice of transmit signaling strategies and sensing channel estimators under different sensing SNRs and ISAC requirements.

TABLE III

GUIDELINES ON WHICH TRANSMIT SIGNALING STRATEGY (QAM OR QPSK) AND CHANNEL ESTIMATOR TO USE UNDER DIFFERENT SNR REGIMES AND ISAC REQUIREMENTS

ISAC Requirement	High P_{d} Low Rate	Medium P_{d} Medium Rate	Low P_{d} High Rate
Low SNR	QPSK/ All Estimators	QAM/ LMMSE+MF	QAM/ LMMSE+MF
High SNR	QPSK/ All Estimators	QAM/ LMMSE	QAM/ LMMSE

D. Concurrent Versus Time-Sharing Transmission

We now carry out a comparative analysis of Concurrent and Time-Sharing strategies, as depicted in Fig. 1 and described in (3) and (4), using the same scenarios in Sec. V-C. Fig. 9 shows the trade-off curves achieved by Time-Sharing[12] as the time-sharing ratio $|\mathcal{S}|/M$ in (4) sweeps the interval $[0, 1]$, along with those belonging to the Concurrent strategy.

The comparison between Concurrent and Time-Sharing strategies reveals the effect of two counteracting factors, each prevailing under distinct operational conditions:

- *C-SNR-Boost: Full Data Utilization for Sensing:* Concurrent (C) strategy leverages the entire OFDM frame for sensing, offering a potential advantage in data utilization

[10]Since all estimators are equivalent under QPSK signaling, as discussed in Sec. III-A4, a single curve is plotted for the case of QPSK.

[11]The steep trade-off curve for QPSK, in contrast to QAM, is attributed to the fact that the rate for QAM reaches its maximum at a higher SNR level than QPSK, leading to a more gradual decrease in P_{d} as the rate increases. Note that as ρ in (3) approaches 0, the sensing SNR decreases and the communication SNR increases.

[12]Since only QPSK pilots are used for sensing in the Time-Sharing strategy(see Sec. II-B.2 and Fig. 1), all sensing algorithms are equivalent.

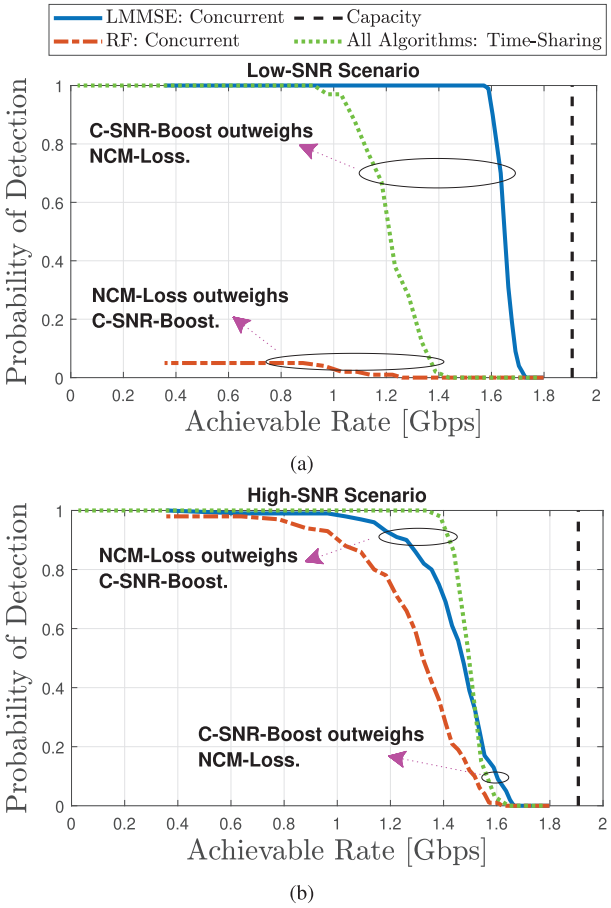

Fig. 9. ISAC trade-off curves under concurrent and time-sharing transmission strategies, where dedicated QPSK pilots are used for sensing in time-sharing and 1024−QAM data are used for communications (see Fig. 1). The time-sharing curves are obtained by sweeping $|\mathcal{S}|/M$ in (4) over $[0, 1]$. (a) Low-SNR sensing scenario for target RCS of 0 dBsm. (b) High-SNR sensing scenario for target-1 RCS of 2 dBsm.

via SNR boosting over Time-Sharing, which limits sensing to dedicated pilots, reducing detection capabilities.

- *NCM-Loss: Impact of Non-Constant-Modulus (NCM) QAM Data on Sensing:* While Concurrent transmission benefits from using QAM data for sensing, this does not guarantee enhanced detection over Time-Sharing. The presence of high side-lobe levels from QAM can be detrimental if the sensing algorithm is ill-equipped to handle them, placing Concurrent at a disadvantage against Time-Sharing, which relies on QPSK pilots for sensing.[13]

For the low-SNR scenario depicted in Fig. 9(a), Concurrent transmission with QAM, in combination with LMMSE at the sensing receiver, yields significantly better ISAC trade-offs than Time-Sharing. This indicates that the full utilization of data for sensing (C-SNR-Boost) outweighs the challenges associated with using QAM data (NCM-Loss) in this scenario, confirming the effectiveness of the proposed LMMSE approach. The allocated sensing pilots in Time-Sharing are not

[13]It is worth emphasizing that the influence of these factors on sensing performance depends on the specific circumstances, suggesting that observed performance patterns may vary with changes in sensing and communication channel characteristics, time/power allocations between the two functionalities and the choice of sensing algorithm, as subsequent discussions will illustrate.

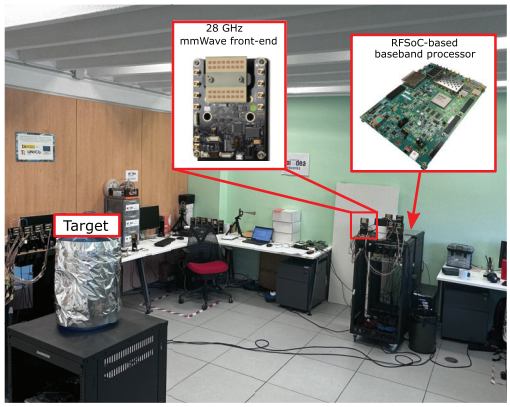

Fig. 10. Experimental setup with the testbed and a single target.

sufficient to achieve P_{d} as high as that achieved by Concurrent for an equivalent rate (corresponding to a certain $|\mathcal{S}|/M$ in Time-Sharing and a certain ρ in Concurrent). Conversely, a scenario where NCM-Loss dominates C-SNR-Boost is seen when comparing the performance of the RF estimator in Concurrent transmission to Time-Sharing. Despite the utilization of the full OFDM frame with QAM data by the RF estimator in Concurrent transmission, it experiences a noticeable reduction in P_{d} compared to Time-Sharing, which relies solely on QPSK pilots for sensing. This disadvantage for RF in Concurrent mode results from increased side-lobe levels at low SNRs, as previously shown in Fig. 2 and Fig. 3.

The high-SNR scenario in Fig. 9(b) reveals trends in ISAC trade-offs that differ considerably from those observed in the low-SNR scenario, which highlights the scenario-specific nature of the relative weights of C-SNR-Boost and NCM-Loss. In this scenario, the high-SNR environment renders the use of dedicated QPSK pilots sufficiently effective for achieving a detection probability (P_{d}) of 1, making the full utilization of OFDM data for sensing (C-SNR-Boost) less critical up to a certain rate threshold. This effect is particularly noticeable until the rate approaches 1.4 Gbps, where P_{d} of 1 is attainable with only a fraction of the transmit symbols dedicated to pilots. A key insight emerges when rates surpass 1.5 Gbps: Concurrent begins to outperform Time-Sharing as the reduced proportion of pilots no longer suffices for maintaining high P_{d} in Time-Sharing. In contrast, exploitation of data in Concurrent provides additional SNR benefits, enhancing detection performance, thereby indicating the dominance of C-SNR-Boost over NCM-Loss in this rate regime. We note that such gains are possible with the use of the proposed LMMSE estimator, which can successfully counteract target masking effects, whereas RF (and, thus MF) with Concurrent transmission is outperformed by Time-Sharing. The threshold at which Concurrent gains an advantage over Time-Sharing varies with the scenario, influenced by the interplay between C-SNR-Boost and NCM-Loss. For instance, Concurrent outperforms Time-Sharing in all rate regimes in the low-SNR scenario.

E. Experimental Results

In this part, to corroborate the findings in Fig. 2 and Fig. 3, we provide experimental results obtained via a full-duplex

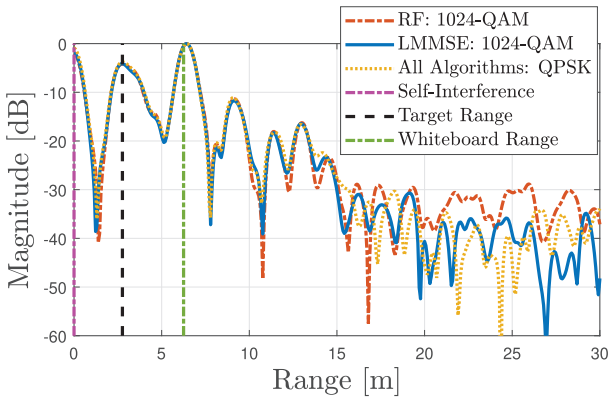

Fig. 11. Range profiles obtained by different channel estimation algorithms with QPSK and 1024-QAM modulations, using real-world experimental data collected via a monostatic full-duplex OFDM radar at $f_c = 28\,\mathrm{GHz}$.

OFDM monostatic sensing setup at IMDEA Network laboratories. The data is collected using the Mimorph testbed from [59], which was enhanced to support fully synchronized and concurrent transmit/receive operation. Millimeter wave front-end is formed by a Sivers IMA EVK operating at the 28 GHz frequency band. The front-end is composed by up/down converters and a 2×8 linear phased antenna array with analog beamforming capabilities. Experiments were collected in a indoor laboratory environment of $6\,\mathrm{m} \times 8\,\mathrm{m}$ with furniture. The testbed was located on one side of the room in the presence of a cylindrical metallic target, as shown in Fig. 10.

Fig. 11 shows the range profiles obtained by the considered algorithms using QPSK and 1024-QAM modulations on experimentally collected data. We observe the peak corresponding to the target at $2.76\,\mathrm{m}$ as well as the self-interference peak resulting from full-duplex operation and the peak due to a large whiteboard located at $6.25\,\mathrm{m}$ in the wall opposite to the testbed. Consistent with Fig. 2 and Fig. 3, the RF estimator produces substantially higher side-lobe levels with QAM modulation compared to QPSK modulation, particularly beyond the $20\,\mathrm{m}$ range. Moreover, the LMMSE estimator with QAM modulation (using $\mathrm{SNR}_b = -20\,\mathrm{dB}$ in (22)) can significantly reduce side-lobe levels and restore the range profile comparable to that achieved with QPSK modulation, in line with insights from Fig. 3.

VI. Concluding Remarks

In this paper, we have investigated two fundamental trade-offs in monostatic OFDM ISAC systems: *(i)* the *time-frequency trade-off*, resulting from the choice of modulation scheme for random data, and *(ii)* the *spatial trade-off*, stemming from how ISAC transmit beamforming is applied to balance sensing and communication objectives. A novel LMMSE based sensing algorithm has been proposed to deal with the increased side-lobe levels induced by high-order QAM data, showcasing substantial improvements over existing OFDM radar sensing benchmarks. Moreover, two ISAC transmission strategies have been considered: *(i) Concurrent*, utilizing all data for sensing with power allocated between sensing and communication beams, and *(ii) Time-Sharing*, where sensing relies solely on dedicated pilots with time-multiplexing for sensing and communication beams. Extensive simulations and experimental results demonstrate the superiority of LMMSE over the conventional RF and MF estimators under a wide range of operating conditions, while unveiling key insights into the ISAC trade-offs achieved by these strategies at different SNRs and modulation schemes. As future research, we intend to focus on the same fundamental trade-offs in bistatic ISAC scenarios. Moreover, we plan to conduct further experimental validation of the proposed method, especially at high SNRs.

Appendix A
Proof of Lemma 1

Using (17), (18) and the definitions in Lemma 1, one can readily obtain $\overline{\mathbf{h}}_{i,b} = \sum_{k=0}^{K-1} \mathbb{E}\{\alpha_{b,k}\}\mathbb{E}\{\mathbf{c}_b^*(\nu_k) \otimes \mathbf{b}(\tau_k)[\mathbf{a}_{\mathrm{R}}(\theta_k)]_i\} = \mathbf{0}$. As to the covariance, we have that

$$\mathbf{C}_{i,b} = \sum_{k_1=1}^{K}\sum_{k_2=1}^{K} \mathbb{E}\{\alpha_{b,k_1}\alpha_{b,k_2}^*\boldsymbol{\phi}_{k_1,b,i}\boldsymbol{\phi}_{k_2,b,i}^H\}\,, \tag{52}$$

where $\boldsymbol{\phi}_{k,b,i} \triangleq \mathbf{c}_b^*(\nu_k) \otimes \mathbf{b}(\tau_k)[\mathbf{a}_{\mathrm{R}}(\theta_k)]_i$. Due to the independence across the different parameters and the different targets, and using the definitions in Lemma 1, (52) simplifies to

$$\begin{aligned}\mathbf{C}_{i,b} &= \sum_{k=0}^{K-1} \mathbb{E}\{|\alpha_{b,k}|^2\}\mathbb{E}\{\boldsymbol{\phi}_{k,b,i}\boldsymbol{\phi}_{k,b,i}^H\}\,,\\ &= \sum_{k=0}^{K-1} \sigma_{\alpha_{b,k}}^2 \mathbb{E}\{\mathbf{c}_b^*(\nu_k)\mathbf{c}_b^T(\nu_k)\} \otimes \mathbb{E}\{\mathbf{b}(\tau_k)\mathbf{b}^H(\tau_k)\}\,,\end{aligned} \tag{53}$$

where the mixed-product property of the Kronecker product is used. Using (13), it follows that $\mathbb{E}\{[\mathbf{b}(\tau_k)\mathbf{b}^H(\tau_k)]_{n,n}\} = 1$ and $\mathbb{E}\left\{\left[\mathbf{b}\left(\tau_k\right)\mathbf{b}^H\left(\tau_k\right)\right]_{n_1,n_2}\right\} = \int_0^{\frac{1}{\Delta f}} e^{j2\pi(n_2-n_1)\Delta f \tau_k}\,\mathrm{d}\tau_k = 0$, for $n_1 \neq n_2$, which yields $\mathbb{E}\{\mathbf{b}(\tau_k)\mathbf{b}^H(\tau_k)\} = \mathbf{I}_N$. Similarly, using (14), we obtain $\mathbb{E}\{\mathbf{c}_b^*(\nu_k)\mathbf{c}_b^T(\nu_k)\} = \mathbf{I}_{M_b}$. Plugging these into (53) gives $\mathbf{C}_{i,b} = \sigma_{\alpha_b}^2\mathbf{I}$.

Appendix B
Proof of Proposition 1

To derive $\chi(\tau,\nu)$ in (23), we consider a target with channel gain α, delay τ_0 and Doppler shift ν_0, and a generic OFDM radar observation matrix

$$\mathbf{Y} = \mathbf{H} \odot \mathbf{X} + \mathbf{N} \in \mathbb{C}^{N\times M}\,, \tag{54}$$

where $\mathbf{H} = \alpha\mathbf{b}(\tau_0)\mathbf{c}^H(\nu_0) \in \mathbb{C}^{N\times M}$ is the radar channel, $\mathbf{X} \in \mathbb{C}^{N\times M}$ is the transmit symbol matrix and $\mathbf{N}$ denotes the noise matrix with $\mathrm{vec}\,(\mathbf{N}) \sim \mathcal{CN}(\mathbf{0}, \sigma^2\mathbf{I})$. The delay-Doppler response for $\mathbf{Y}$ in (54) is obtained as in (31), i.e.,

$$\chi(\tau,\nu) = \frac{1}{NM}\mathbf{b}^H(\tau)(\mathbf{Y}\odot\mathbf{G})\mathbf{c}(\nu)\,, \tag{55}$$

where $\mathbf{Y}\odot\mathbf{G}$ represents the radar channel estimate obtained using RF, MF or LMMSE estimators in (15), (16) and (22),

$$\mathbf{G} = \begin{cases} \dfrac{\mathbf{X}^*}{|\mathbf{X}|^2}\,, & \text{RF}\\ \mathbf{X}^*\,, & \text{MF}\\ \dfrac{\mathbf{X}^*}{|\mathbf{X}|^2 + \mathrm{SNR}^{-1}}\,, & \text{LMMSE}\end{cases}\,, \tag{56}$$

and $\mathrm{SNR} = |\alpha|^2/\sigma^2$. Inserting (54) into (55) yields $\chi(\tau,\nu) = \chi_{\mathrm{s}}(\tau,\nu) + \chi_{\mathrm{n}}(\tau,\nu)$, where $\chi_{\mathrm{s}}(\tau,\nu)$ and $\chi_{\mathrm{n}}(\tau,\nu)$ represent the signal and noise part of the delay-Doppler response, i.e.,

$$\chi_{\mathrm{s}}(\tau,\nu) \triangleq \frac{1}{NM}\alpha \mathbf{b}^H(\tau)\left(\mathbf{b}(\tau_0)\mathbf{c}^H(\nu_0)\odot\mathbf{X}\odot\mathbf{G}\right)\mathbf{c}(\nu)\,,$$
$$\chi_{\mathrm{n}}(\tau,\nu) \triangleq \frac{1}{NM}\mathbf{b}^H(\tau)\left(\mathbf{N}\odot\mathbf{G}\right)\mathbf{c}(\nu)\,.$$

The average delay-Doppler response is then given by

$$\mathbb{E}\{|\chi(\tau,\nu)|^2\} = \mathbb{E}\{|\chi_{\mathrm{s}}(\tau,\nu)|^2\} + \mathbb{E}\{|\chi_{\mathrm{n}}(\tau,\nu)|^2\} + 2\Re\left\{\mathbb{E}\{\chi_{\mathrm{s}}(\tau,\nu)\chi_{\mathrm{n}}^*(\tau,\nu)\}\right\}\,. \quad (57)$$

We present the following auxiliary lemmas to compute (57).

Lemma 2: The signal component in (57) at the main-lobe peak and in the asymptotic side-lobe region $\mathcal{R}$ can be expressed as

$$\mathbb{E}\{|\chi_{\mathrm{s}}(\tau_0,\nu_0)|^2\} = \frac{|\alpha|^2\left(\beta_x + (NM-1)\mu_x\right)}{NM}\,, \quad (58)$$
$$\mathbb{E}\{|\chi_{\mathrm{s}}(\tau,\nu)|^2\} = \frac{|\alpha|^2(\beta_x-\mu_x)}{NM}\,, \quad (\tau,\nu)\in\mathcal{R}\,, \quad (59)$$

where

$$\beta_x \triangleq \begin{cases} 1\,, & \text{RF} \\ \mathbb{E}\{|x|^4\}\,, & \text{MF} \\ \mathbb{E}\left\{\dfrac{|x|^4}{(|x|^2+\mathrm{SNR}^{-1})^2}\right\}\,, & \text{LMMSE,} \end{cases} \quad (60)$$

$$\mu_x \triangleq \begin{cases} 1\,, & \text{RF} \\ \left(\mathbb{E}\{|x|^2\}\right)^2\,, & \text{MF} \\ \left(\mathbb{E}\left\{\dfrac{|x|^2}{|x|^2+\mathrm{SNR}^{-1}}\right\}\right)^2\,, & \text{LMMSE.} \end{cases} \quad (61)$$

Proof: The proof relies on the fact that we consider a sufficiently large N and M to ensure $(\tau,\nu)\in\mathcal{R}$ in (59), i.e., $|\tau-\tau_0| \gg \Delta\tau = 1/(N\Delta f)$ and $|\nu-\nu_0| \gg \Delta\nu = 1/(MT_{\mathrm{sym}})$. Utilizing the limits $\lim_{N\to\infty}\left(\frac{\sin(\pi N\Delta f\tau)}{N\sin(\pi\Delta f\tau)}\right)^2 = 0$ and $\lim_{M\to\infty}\left(\frac{\sin(\pi MT_{\mathrm{sym}}\nu)}{M\sin(\pi T_{\mathrm{sym}}\nu)}\right)^2 = 0$, and through algebraic manipulations, we derive the equations (58) and (59). The detailed steps are omitted due to space constraints. ∎

Lemma 3: The noise component in (57) is given by

$$\mathbb{E}\{|\chi_{\mathrm{n}}(\tau,\nu)|^2\} = \frac{\sigma^2\kappa_x}{NM}\,, \quad (62)$$

where

$$\kappa_x \triangleq \begin{cases} \mathbb{E}\left\{\dfrac{1}{|x|^2}\right\}\,, & \text{RF} \\ \mathbb{E}\{|x|^2\}\,, & \text{MF} \\ \mathbb{E}\left\{\dfrac{|x|^2}{(|x|^2+\mathrm{SNR}^{-1})^2}\right\}\,, & \text{LMMSE.} \end{cases} \quad (63)$$

Proof: The proof follows readily from the independence of the transmit symbols $\mathbf{X}$ and the noise $\mathbf{N}$. ∎

Lemma 4: The cross-term in (57) is given by

$$\mathbb{E}\{\chi_{\mathrm{s}}(\tau,\nu)\chi_{\mathrm{n}}^*(\tau,\nu)\} = 0\,. \quad (64)$$

Proof: The proof is obtained similarly to that of Lemma 3. ∎

Using Lemmas 2–4 in (57) and considering $\mathbb{E}\{|x|^2\}=1$, the PSLR in (23) evaluates to (24), (25) and (26) for the RF, MF and LMMSE estimators, respectively.

Appendix C
Proof of Proposition 2

By Jensen's inequality and the convexity of $1/x$,

$$\left(\mathbb{E}\left\{\frac{|x|^2}{|x|^2+\mathrm{SNR}^{-1}}\right\}\right)^{-1} \le 1 + \mathbb{E}\left\{\frac{1}{|x|^2}\right\}\mathrm{SNR}^{-1}\,. \quad (65)$$

Inserting this into (26) yields the desired result.

Appendix D
Proof of Proposition 3

By the Cauchy-Schwarz inequality,

$$\mathbb{E}\left\{|x|^2(|x|^2+\mathrm{SNR}^{-1})\right\}\mathbb{E}\left\{\frac{|x|^2}{|x|^2+\mathrm{SNR}^{-1}}\right\} \ge \left(\mathbb{E}\left\{|x|^2\right\}\right)^2\,.$$

Inserting $\mathbb{E}\left\{|x|^2\right\}=1$, we obtain

$$\mathbb{E}\left\{|x|^4\right\} + \mathrm{SNR}^{-1} \ge \left(\mathbb{E}\left\{\frac{|x|^2}{|x|^2+\mathrm{SNR}^{-1}}\right\}\right)^{-1}\,,$$

which leads to the desired result based on (25) and (26).

Appendix E
Proof of Corollary 2

By Jensen's inequality and the convexity of $1/x$ and x^2, $\mathbb{E}\left\{\frac{1}{|x|^2}\right\} \ge \frac{1}{\mathbb{E}\{|x|^2\}} = 1$ and $\mathbb{E}\left\{|x|^4\right\} \ge \left(\mathbb{E}\left\{|x|^2\right\}\right)^2 = 1$, with equality if and only if $|x|^2$ is a constant. Hence, $\mathrm{PSLR}^{\mathrm{RF}}$ and $\mathrm{PSLR}^{\mathrm{MF}}$ achieve their highest values with PSK modulation and decrease with varying-amplitude modulations.

References

[1] F. Liu, C. Masouros, A. P. Petropulu, H. Griffiths, and L. Hanzo, "Joint radar and communication design: Applications, state-of-the-art, and the road ahead," *IEEE Trans. Commun.*, vol. 68, no. 6, pp. 3834–3862, Jun. 2020.

[2] J. A. Zhang et al., "Enabling joint communication and radar sensing in mobile networks—A survey," *IEEE Commun. Surveys Tuts.*, vol. 24, no. 1, pp. 306–345, 1st Quart., 2022.

[3] F. Liu et al., "Seventy years of radar and communications: The road from separation to integration," *IEEE Signal Process. Mag.*, vol. 40, no. 5, pp. 106–121, Jul. 2023.

[4] F. Liu et al., "Integrated sensing and communications: Toward dual-functional wireless networks for 6G and beyond," *IEEE J. Sel. Areas Commun.*, vol. 40, no. 6, pp. 1728–1767, Jun. 2022.

[5] F. Dong, F. Liu, Y. Cui, S. Lu, and Y. Li, "Sensing as a service in 6G perceptive mobile networks: Architecture, advances, and the road ahead," *IEEE Netw.*, vol. 38, no. 2, pp. 87–96, Mar. 2024.

[6] L. Pucci, E. Paolini, and A. Giorgetti, "System-level analysis of joint sensing and communication based on 5G new radio," *IEEE J. Sel. Areas Commun.*, vol. 40, no. 7, pp. 2043–2055, Jul. 2022.

[7] C. Baquero Barneto et al., "Full-duplex OFDM radar with LTE and 5G NR waveforms: Challenges, solutions, and measurements," *IEEE Trans. Microw. Theory Techn.*, vol. 67, no. 10, pp. 4042–4054, Oct. 2019.

[8] M. F. Keskin, H. Wymeersch, and V. Koivunen, "Monostatic sensing with OFDM under phase noise: From mitigation to exploitation," *IEEE Trans. Signal Process.*, vol. 71, pp. 1363–1378, 2023.

[9] J. Pegoraro et al., "JUMP: Joint communication and sensing with unsynchronized transceivers made practical," *IEEE Trans. Wireless Commun.*, vol. 23, no. 8, pp. 9759–9775, Aug. 2024.

[10] X. Lin, "An overview of 5G advanced evolution in 3GPP release 18," *IEEE Commun. Standards Mag.*, vol. 6, no. 3, pp. 77–83, Sep. 2022.

[11] C. Sturm and W. Wiesbeck, "Waveform design and signal processing aspects for fusion of wireless communications and radar sensing," *Proc. IEEE*, vol. 99, no. 7, pp. 1236–1259, Jul. 2011.

[12] F. Zhang, Z. Zhang, W. Yu, and T.-K. Truong, "Joint range and velocity estimation with intrapulse and intersubcarrier Doppler effects for OFDM-based RadCom systems," *IEEE Trans. Signal Process.*, vol. 68, pp. 662–675, 2020.

[13] M. F. Keskin, V. Koivunen, and H. Wymeersch, "Limited feedforward waveform design for OFDM dual-functional radar-communications," *IEEE Trans. Signal Process.*, vol. 69, pp. 2955–2970, Apr. 2021.

[14] Z. Du, F. Liu, Y. Xiong, T. X. Han, Y. C. Eldar, and S. Jin, "Reshaping the ISAC tradeoff under OFDM signaling: A probabilistic constellation shaping approach," *IEEE Trans. Signal Process.*, vol. 72, pp. 4782–4797, 2024.

[15] Z. Wei et al., "5G PRS-based sensing: A sensing reference signal approach for joint sensing and communication system," *IEEE Trans. Veh. Technol.*, vol. 72, no. 3, pp. 3250–3263, Mar. 2023.

[16] Y. Li, F. Liu, Z. Du, W. Yuan, Q. Shi, and C. Masouros, "Frame structure and protocol design for sensing-assisted NR-V2X communications," *IEEE Trans. Mobile Comput.*, vol. 23, no. 12, pp. 11045–11060, Dec. 2024.

[17] A. Ksiezyk et al., "Opportunities and limitations in radar sensing based on 5G broadband cellular networks," *IEEE Aerosp. Electron. Syst. Mag.*, vol. 38, no. 9, pp. 4–21, Sep. 2023.

[18] Z. Wei et al., "A 5G DMRS-based signal for integrated sensing and communication system," 2023, *arXiv:2312.02170*.

[19] Z. Xiao, R. Liu, M. Li, Q. Liu, and A. Lee Swindlehurst, "A novel joint angle-range-velocity estimation method for MIMO-OFDM ISAC systems," 2023, *arXiv:2308.03387*.

[20] S. Mura, D. Tagliaferri, M. Mizmizi, U. Spagnolini, and A. Petropulu, "Optimized waveform design for OFDM-based ISAC systems under limited resource occupancy," 2024, *arXiv:2406.19036*.

[21] P. Li, M. Li, R. Liu, Q. Liu, and A. Lee Swindlehurst, "MIMO-OFDM ISAC waveform design for range-Doppler sidelobe suppression," 2024, *arXiv:2406.17218*.

[22] Y. Lai, M. F. Keskin, H. Wymeersch, L. Venturino, W. Yi, and L. Kong, "Subspace-based detection in OFDM ISAC systems under different constellations," in *Proc. IEEE Int. Conf. Acoust., Speech Signal Process. (ICASSP)*, Apr. 2024, pp. 9126–9130.

[23] Y. Xiong, F. Liu, and M. Lops, "Generalized deterministic-random tradeoff of integrated sensing and communications: The sensing-optimal operating point," in *Proc. IEEE Int. Conf. Acoust., Speech Signal Process. (ICASSP)*, Apr. 2024, pp. 8481–8485.

[24] Y. Zhang, S. Aditya, and B. Clerckx, "Input distribution optimization in OFDM dual-function radar-communication systems," 2023, *arXiv:2305.06635*.

[25] S. Lu, F. Liu, F. Dong, Y. Xiong, J. Xu, and Y.-F. Liu, "Sensing with random signals," 2023, *arXiv:2309.02375*.

[26] Y. Xiong, F. Liu, Y. Cui, W. Yuan, T. X. Han, and G. Caire, "On the fundamental tradeoff of integrated sensing and communications under Gaussian channels," *IEEE Trans. Inf. Theory*, vol. 69, no. 9, pp. 5723–5751, Sep. 2023.

[27] S. Mercier, S. Bidon, D. Roque, and C. Enderli, "Comparison of correlation-based OFDM radar receivers," *IEEE Trans. Aerosp. Electron. Syst.*, vol. 56, no. 6, pp. 4796–4813, Dec. 2020.

[28] E. Grossi, M. Lops, and L. Venturino, "Adaptive detection and localization exploiting the IEEE 802.11ad standard," *IEEE Trans. Wireless Commun.*, vol. 19, no. 7, pp. 4394–4407, Jul. 2020.

[29] A. Bazzi and M. Chafii, "On outage-based beamforming design for dual-functional radar-communication 6G systems," *IEEE Trans. Wireless Commun.*, vol. 22, no. 8, pp. 5598–5612, Aug. 2023.

[30] M. Ahmadipour, M. Kobayashi, M. Wigger, and G. Caire, "An information-theoretic approach to joint sensing and communication," *IEEE Trans. Inf. Theory*, vol. 70, no. 2, pp. 1124–1146, Feb. 2024.

[31] Z. Xu and A. Petropulu, "A bandwidth efficient dual-function radar communication system based on a MIMO radar using OFDM waveforms," *IEEE Trans. Signal Process.*, vol. 71, pp. 401–416, 2023.

[32] Z. Zhang, X. Chai, K. Long, A. V. Vasilakos, and L. Hanzo, "Full duplex techniques for 5G networks: Self-interference cancellation, protocol design, and relay selection," *IEEE Commun. Mag.*, vol. 53, no. 5, pp. 128–137, May 2015.

[33] M. Braun, "OFDM radar algorithms in mobile communication networks," Karlsruher Institutes für Technologie, Karlsruhe, Germany, Tech. Rep., 2014, doi: 10.5445/IR/1000038892.

[34] P. Kumari, J. Choi, N. González-Prelcic, and R. W. Heath Jr., "IEEE 802.11ad-based radar: An approach to joint vehicular communication-radar system," *IEEE Trans. Veh. Technol.*, vol. 67, no. 4, pp. 3012–3027, Apr. 2018.

[35] S. D. Liyanaarachchi, T. Riihonen, C. B. Barneto, and M. Valkama, "Optimized waveforms for 5G-6G communication with sensing: Theory, simulations and experiments," *IEEE Trans. Wireless Commun.*, vol. 20, no. 12, pp. 8301–8315, Dec. 2021.

[36] M. F. Keskin, H. Wymeersch, and V. Koivunen, "MIMO-OFDM joint radar-communications: Is ICI friend or foe?," *IEEE J. Sel. Topics Signal Process.*, vol. 15, no. 6, pp. 1393–1408, Nov. 2021.

[37] J. A. Zhang, X. Huang, Y. J. Guo, J. Yuan, and R. W. Heath Jr., "Multibeam for joint communication and radar sensing using steerable analog antenna arrays," *IEEE Trans. Veh. Technol.*, vol. 68, no. 1, pp. 671–685, Jan. 2019.

[38] M. B. Salman, Ö. T. Demir, and E. Björnson, "When are sensing symbols required for ISAC?," *IEEE Trans. Veh. Technol.*, vol. 73, no. 10, pp. 15709–15714, Oct. 2024.

[39] J. A. Zhang et al., "An overview of signal processing techniques for joint communication and radar sensing," *IEEE J. Sel. Topics Signal Process.*, vol. 15, no. 6, pp. 1295–1315, Nov. 2021.

[40] M. A. Richards, *Fundamentals of Radar Signal Processing*. New York, NY, USA: McGraw-Hill, 2005.

[41] Z. Abu-Shaban, X. Zhou, T. Abhayapala, G. Seco-Granados, and H. Wymeersch, "Error bounds for uplink and downlink 3D localization in 5G millimeter wave systems," *IEEE Trans. Wireless Commun.*, vol. 17, no. 8, pp. 4939–4954, Aug. 2018.

[42] F. Liu, W. Yuan, C. Masouros, and J. Yuan, "Radar-assisted predictive beamforming for vehicular links: Communication served by sensing," *IEEE Trans. Wireless Commun.*, vol. 19, no. 11, pp. 7704–7719, Nov. 2020.

[43] G. Hakobyan, M. Ulrich, and B. Yang, "OFDM-MIMO radar with optimized nonequidistant subcarrier interleaving," *IEEE Trans. Aerosp. Electron. Syst.*, vol. 56, no. 1, pp. 572–584, Feb. 2020.

[44] M. F. Keskin, C. Marcus, O. Eriksson, A. Alvarado, J. Widmer, and H. Wymeersch, "Integrated sensing and communications with MIMO-OTFS: ISI/ICI exploitation and delay-Doppler multiplexing," *IEEE Trans. Wireless Commun.*, vol. 23, no. 8, pp. 10229–10246, Aug. 2024.

[45] J.-J. Van De Beek, O. Edfors, M. Sandell, S. K. Wilson, and P. O. Borjesson, "On channel estimation in OFDM systems," in *Proc. IEEE 45th Veh. Technol. Conf.*, vol. 2, Jul. 1995, pp. 815–819.

[46] K. Fazel, *Multi-Carrier and Spread Spectrum Systems: From OFDM and MC-CDMA to LTE and WiMAX*. Hoboken, NJ, USA: Wiley, 2008.

[47] J. T. Rodriguez, F. Colone, and P. Lombardo, "Supervised reciprocal filter for OFDM radar signal processing," *IEEE Trans. Aerosp. Electron. Syst.*, vol. 59, no. 4, pp. 3871–3889, Jun. 2023.

[48] S. M. Kay, *Fundamentals of Statistical Signal Processing: Estimation Theory*. Upper Saddle River, NJ, USA: Prentice-Hall, 1993.

[49] A. Aubry, A. D. Maio, V. Carotenuto, and A. Farina, "Radar phase noise modeling and effects-part I: MTI filters," *IEEE Trans. Aerosp. Electron. Syst.*, vol. 52, no. 2, pp. 698–711, Apr. 2016.

[50] L. Gaudio, M. Kobayashi, G. Caire, and G. Colavolpe, "On the effectiveness of OTFS for joint radar parameter estimation and communication," *IEEE Trans. Wireless Commun.*, vol. 19, no. 9, pp. 5951–5965, Sep. 2020.

[51] A. W. Azim, A. Bazzi, R. Shubair, and M. Chafii, "Dual-mode chirp spread spectrum modulation," *IEEE Wireless Commun. Lett.*, vol. 11, no. 9, pp. 1995–1999, Sep. 2022.

[52] N. Neuberger and R. Vehmas, "Range sidelobe level reduction with a train of diverse LFM pulses," *IEEE Trans. Aerosp. Electron. Syst.*, vol. 58, no. 2, pp. 1480–1486, Apr. 2022.

[53] T. Kazaz, G. J. M. Janssen, J. Romme, and A.-J. van der Veen, "Delay estimation for ranging and localization using multiband channel state information," *IEEE Trans. Wireless Commun.*, vol. 21, no. 4, pp. 2591–2607, Apr. 2022.

[54] Y. Ge, M. Stark, M. F. Keskin, F. Hofmann, T. Hansen, and H. Wymeersch, "V2X sidelink positioning in FR1: Scenarios, algorithms, and performance evaluation," *IEEE J. Sel. Areas Commun.*, vol. 42, no. 10, pp. 2608–2624, Oct. 2024.

[55] M. Ester, H.-P. Kriegel, J. Sander, and X. Xu, "A density-based algorithm for discovering clusters in large spatial databases with noise," *Proc. KDD*, Aug. 1996, vol. 96, no. 34, pp. 226–231.

[56] R. He et al., "Clustering enabled wireless channel modeling using big data algorithms," *IEEE Commun. Mag.*, vol. 56, no. 5, pp. 177–183, May 2018.

[57] S. H. Song and Q. T. Zhang, "Mutual information of multipath channels with imperfect channel information," *IEEE Trans. Commun.*, vol. 57, no. 5, pp. 1523–1531, May 2009.
[58] M. Thomas, *Elements of Information Theory*. Hoboken, NJ, USA: Wiley, 2006.
[59] J. O. Lacruz, R. R. Ortiz, and J. Widmer, "A real-time experimentation platform for sub-6 GHz and millimeter-wave MIMO systems," in *Proc. 19th Annu. Int. Conf. Mobile Syst., Appl., Services*, Jun. 2021, pp. 427–439.

Musa Furkan Keskin (Member, IEEE) received the Ph.D. degree in electrical and electronics engineering from Bilkent University, Ankara, Türkiye, in 2018. He is currently a Research Specialist with the Department of Electrical Engineering, Chalmers University of Technology, Gothenburg, Sweden, where he is leading and contributing to various interdisciplinary and industry-focused research projects at both Swedish and European levels, with a specialization in integrated localization, communication, and sensing in 6G systems. His awards include the 2019 IEEE Turkey Best Ph.D. Thesis Award for his work on visible light positioning systems, the EU MSCA Postdoctoral Fellowship for his project "OTFS-RADCOM: A New Waveform for Joint Radar and Communications Beyond 5G," and the Swedish Research Council (VR) Starting Grant for his project on "Localization and Sensing for Perceptive Cell-Free Networks Towards 6G." He serves as an Editor for IEEE TRANSACTIONS ON COMMUNICATIONS and IEEE TRANSACTIONS ON MOBILE COMPUTING.

Mohammad Mahdi Mojahedian (Member, IEEE) received the dual B.Sc. degree in communications and electronics from the Amirkabir University of Technology (Tehran Polytechnic), Tehran, Iran, in 2009 and 2010, respectively, the M.Sc. degree in communication systems from the Sharif University of Technology in 2012, the Ph.D. degree from the Communication Systems Group, Sharif University of Technology, in 2018. Since 2012, he has been affiliated with the Information Systems and Security Laboratory (ISSL), Sharif University. He is currently engaged in collaborative research with the Sharif University of Technology and the Chalmers University of Technology. His research interests include information theory, wireless communications, statistical learning theory, and computer science. In 2015, he was a finalist for the Jack Keil Wolf Student Paper Award at the ISIT Symposium.

Jesus O. Lacruz received the bachelor's degree in electrical engineering from the Universidad de Los Andes, Venezuela, in 2009, and the Ph.D. degree in electronic engineering from Universidad Politécnica de Valencia, Spain, in 2016. He has been a Senior Researcher with IMDEA Networks, Spain, since 2017. His research interests include embedded wireless system design for wireless communication and sensing applications.

Carina Marcus received the M.Sc. degree in electrical engineering from Chalmers, Sweden, in 1995, and the Licentiate Engineering degree in theoretical physics and the Ph.D. degree in theoretical and computational physics from Linköping University, Sweden, in 2004 and 2020, respectively.

She is currently working for Magna Sweden AB as a Research Specialist specializing in Electromagnetic Sensing. Previously, she has held positions with Saab, Sweden, working with sensor and signature aspects of aircraft conceptual design, electromagnetic computations, and radar systems for industrial fluid level gauging. Her interests include radar, EO/IR sensors, the design of multisensor systems, and communication capabilities.

Olof Eriksson is currently a Research Consultant. He has more than 20 years of automotive safety and sensor system experience, working with international companies Saab, Autoliv, Veoneer, and Magna.

Andrea Giorgetti (Senior Member, IEEE) received the Dr.-Ing. degree (summa cum laude) in electronic engineering and the Ph.D. degree in electronic engineering and computer science from the University of Bologna, Bologna, Italy, in 1999 and 2003, respectively. From 2003 to 2005, he was a Researcher with the National Research Council of Italy. In 2006, he joined the Department of Electrical, Electronic, and Information Engineering "Guglielmo Marconi," University of Bologna, as an Assistant Professor and became an Associate Professor in 2014. In Spring 2006, he was with the Laboratory for Information and Decision Systems, Massachusetts Institute of Technology (MIT), Cambridge, MA, USA. He is the co-author of *Cognitive Radio Techniques: Spectrum Sensing, Interference Mitigation, and Localization* (Artech House, 2012). His research interests include ultra-wide bandwidth communication systems, active and passive localization, wireless sensor networks, cognitive radio, and integrated sensing and communications. He has served as the Technical Program Committee Co-Chair for several symposia at IEEE ICC and IEEE GLOBECOM. From 2017 to 2018, he was the Elected Chair of the IEEE Communications Society's Radio Communications Technical Committee. He is a Former Editor of IEEE COMMUNICATIONS LETTERS and IEEE TRANSACTIONS ON WIRELESS COMMUNICATIONS.

Joerg Widmer (Fellow, IEEE) is currently a Research Professor and the Research Director of IMDEA Networks, Madrid, Spain, where he leads the Wireless Networking Research Group. Before, he held positions with DOCOMO Euro-Laboratories, Munich, Germany, and EPFL, Switzerland. He was a Visiting Researcher with the International Computer Science Institute in Berkeley, USA, University College London, U.K., and TU Darmstadt, Germany. He has authored more than 250 conference and journal papers and three IETF RFCs and holds 14 patents. His research focuses on wireless networks, ranging from extremely high-frequency millimeter-wave communication, and wireless sensing to mobile network architectures. He was awarded an ERC consolidator grant, the Friedrich Wilhelm Bessel Research Award of the Alexander von Humboldt Foundation, a Mercator Fellowship of the German Research Foundation, a Spanish Ramon y Cajal grant, as well as fourteen best paper awards. He is a Distinguished Member of ACM.

Henk Wymeersch (Fellow, IEEE) received the Ph.D. degree in electrical engineering/applied sciences from Ghent University, Belgium, in 2005. He is currently a Professor of communication systems with the Department of Electrical Engineering, Chalmers University of Technology, Sweden. Prior to joining Chalmers, he was a Post-Doctoral Researcher with the Laboratory for Information and Decision Systems, Massachusetts Institute of Technology, from 2005 to 2009. His current research interests include the convergence of communication and sensing, in a 5G and beyond 5G context. He is a Senior Member of *IEEE Signal Processing Magazine* Editorial Board. He served as an Associate Editor for IEEE COMMUNICATIONS LETTERS, IEEE TRANSACTIONS ON WIRELESS COMMUNICATIONS, and IEEE TRANSACTIONS ON COMMUNICATIONS. From 2019 to 2021, he was an IEEE Distinguished Lecturer with the Vehicular Technology Society.